



# Modeling CO<sub>2</sub>-Induced Alterations in Mt. Simon Sandstone via Nanomechanics

Ange-Therese Akono<sup>1</sup> · Pooyan Kabir<sup>2</sup> · Zhuofan Shi<sup>3</sup> · Samantha Fuchs<sup>4</sup> · Theodore T. Tsotsis<sup>3</sup> · Kristian Jessen<sup>3</sup> · Charles J. Werth<sup>4</sup>

Received: 29 December 2017 / Accepted: 7 November 2018 / Published online: 10 December 2018  
© Springer-Verlag GmbH Austria, part of Springer Nature 2018

## Abstract

The objective of this work is to formulate a novel and physics-based nanomechanics framework to connect geochemical reactions in host rock to the resulting morphological changes at the microscopic lengthscale and to the resulting geomechanical changes at the macroscopic lengthscale. The key idea is to monitor the fraction of minerals based on their mechanical signature. We illustrate this procedure on the Mt. Simon sandstone from the Illinois Basin. To this end, various acidic fluid systems were applied to Mt. Simon sandstone specimens. The chemistry, morphology, microstructure, and mechanical characteristics were investigated across multiple lengthscales. Grid indentation was carried out with a total of 6900 individual indentation tests performed on 24 specimens. A good agreement was observed between the composition computed using statistical nanoindentation and measurements employing independent methods such as scanning electron microscopy, electron-dispersive X-ray spectroscopy, X-ray diffraction analyses, mercury intrusion porosimetry, flow perporometry, and helium pycnometry. An increase in porosity and a decrease in K-feldspar content were observed following the incubation in CO<sub>2</sub>-saturated brine, suggesting dissolution reactions involving feldspar. Thus, a rigorous methodology is presented to connect geochemical reactions and related compositional changes at the nano- and microscopic scales to alterations of the constitutive behavior at the macroscopic level.

**Keywords** Geochemical reactions · Induced seismicity · Geological carbon sequestration · Sandstone · Multiscale modeling · Statistical nanoindentation

## 1 Introduction

Despite progress in the current understanding of chemo-mechanical interactions in host rock materials, novel multi-scale approaches are needed to connect geochemical reactions to the resulting alterations in geomechanical behavior. Most experiments have been confined to the macroscopic scale to investigate geomechanical alterations based on triaxial testing (Bemer and Lombard 2010), 2D digital image correlation (Zinsmeister et al. 2013), and uniaxial compression tests (Nover et al. 2013; Rimmelé et al. 2010). Overall, it was found that geochemical reactions result in a decrease in transport (Bemer and Lombard 2010) and mechanical properties (Vialle and Vanorio 2011; Xie et al. 2011; Zinsmeister et al. 2013). However, what is lacking is a rigorous and quantitative link between geochemical reactions and geomechanical alterations. A main limitation of prior approaches is that they cannot quantify the microstructural and compositional changes due to geochemical reactions. As

---

✉ Ange-Therese Akono  
ange-therese.akono@northwestern.edu

<sup>1</sup> Department of Civil and Environmental Engineering, Northwestern University, 2145 N Sheridan Rd, Evanston, IL, USA

<sup>2</sup> Department of Civil and Environmental Engineering, University of Illinois at Urbana-Champaign, 205 N. Mathews Avenue, Urbana, IL, USA

<sup>3</sup> Department of Chemical Engineering and Material Science, University of Southern California-Los Angeles, 216 Hedco Building, Los Angeles, CA, USA

<sup>4</sup> Department of Civil, Architectural and Environmental Engineering, University of Texas at Austin, 301 E Dean Keeton St, Austin, TX, USA

a result, the resulting changes in macroscopic mechanical properties can seldom be predicted. Thus, new methods are needed that can monitor changes in local morphology and composition following geochemical reactions, and that can connect these changes to the evolution of the macroscopic mechanical response.

Description of the mathematical symbols used in this study

Symbol	Physical meaning
$A$	Projected contact area at unloading
$\alpha$	Particle aspect ratio
$c_j$	Volume fraction of phase $j$
$E_s$	Young's modulus of solid skeleton at nanoscale
$d$	Penetration depth
$G^{\text{hom}}$	macroscopic shear modulus
$H$	indentation hardness
$K^{\text{hom}}$	Macroscopic bulk modulus
$M$	Indentation modulus
$\eta_j$	Packing density of phase $j$
$\nu_s$	Poisson's ratio
$P$	Vertical load
$P_{\text{max}}$	Maximum vertical force
$\Delta p$	Prescribed pressure drop in flow perporometry experiment
$\phi$	Total porosity
$\varphi$	Nanoporosity
$r$	Pore radius
$S$	Unloading contact stiffness
$\sigma$	Liquid surface tension
$\theta$	Liquid surface contact angle
$\mathbf{X}$	Vector of mechanical characteristics

First, there is a lack of advanced physics-based mathematical models that can correlate chemically-induced morphological alterations to global changes in mechanical properties of geomaterials. Previous studies are based on simplistic representations of the microstructure, which are disconnected from the physical characteristics of real host rocks. Some common simplifying assumptions include the assumption of spherical grains (Bemer et al. 2004; Sun et al. 2016), the assumption of a homogeneous mineral phase (Arson and Vanorio 2015; Nguyen et al. 2011; Sun et al. 2016), and the omission of nanopores (Arson and Vanorio 2015; Sun et al. 2016). The challenge consists of accounting for the multiscale nature of reservoir rocks, their heterogeneity, and the difference in morphology between different constituents. In summary, novel models are needed that can simultaneously account for the two-scale porosity, the aspect ratio of grains, and the heterogeneous mineral phase.

Second, current methods to monitor rock–fluid geochemical reactions do not allow the quantitative prediction of the geomechanical changes that these chemical reactions generate.

Rock–fluid geochemical reactions can be determined using several routes: scanning electron microscopy post-imaging of reacted rock specimens (Liteanu and Spiers 2009; Vanorio et al. 2015), electron-dispersive X-ray fluorescence analyses (Marbler et al. 2013), X-ray diffraction (Rathnaweera et al. 2015), and thermodynamics-based geochemical modeling (Yoksoulia et al. 2013). Although the first three methods only provide qualitative information regarding chemical reactions, the last method is the most commonly employed tool to obtain quantitative information regarding the reaction kinetics—reaction rates, equilibrium constants, mineral activity coefficients, etc. (Bethke 1996; Gautier et al. 1994). However, the predicted dissolution/precipitation rates can be highly inaccurate as the reactive surface area is not always known and equilibrium is not always guaranteed (White and Brantley 2003). Furthermore, thermodynamic calculations only yield a limited understanding of chemically-induced morphological changes and thus are not yet able to predict the observed macroscopic changes in mechanical response. Therefore, a new approach is needed to relate geochemical reactions to macroscopic changes in mechanical behavior.

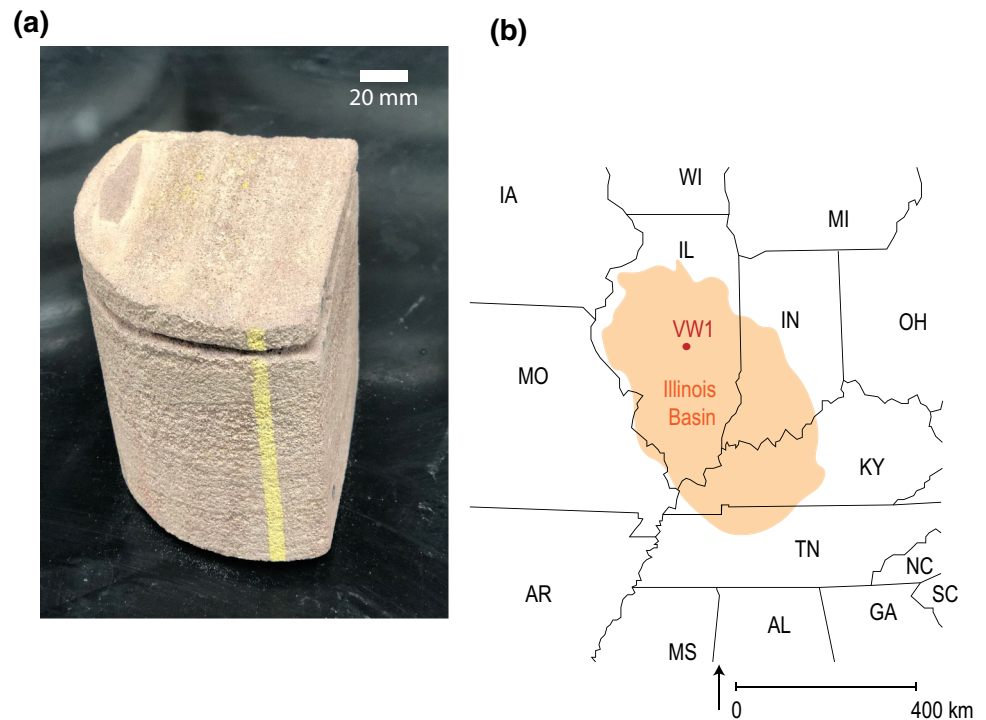
In this study, we introduce a new approach: by monitoring the mechanical signature of silicate minerals—via theoretical and experimental nanomechanics—we connect chemically-induced changes in geochemistry and morphology to the elasto-plastic behavior at the nano-, micro-, and macroscopic lengthscales. We focus our study on the rock cores extracted from the Mt. Simon sandstone formation in the Illinois Basin. Rock specimens were altered using different acidic fluid systems, such as brine and brine–CO<sub>2</sub> mixtures, under various temperature and pressure conditions. The chemistry and microstructure were characterized using advanced analytical methods (scanning electron microscopy, environmental scanning electron microscopy, X-ray diffraction analysis, and energy-dispersive spectroscopy) and porosity measurement techniques (mercury intrusion porosimetry, flow perporometry, and helium pycnometry). Grid nanoindentation was carried out before and after incubation. Statistical deconvolution methods were used to monitor changes in chemical microconstituents. Micromechanics theory was used to relate the microscale behavior to the macroscopic elastic constants. Thus, we formulate here a rigorous and physics-based multiscale framework to understand fluid–rock chemical reactions and their influence on the constitutive behavior.

## 2 Materials and Methods

### 2.1 Mt. Simon Sandstone Formation

The Mt. Simon sandstone is the host formation for the current pilot study on CO<sub>2</sub> storage at the Illinois Basin Decatur Project (IBDP). This site is located in Decatur, Illinois,

**Fig. 1** **a** Digital photograph of the Mt. Simon sandstone 6925 ft core in its unaltered state. Credit: Ange-Therese Akono, Northwestern University, 2018. **b** Illinois Basin map with location of Verification Well 1 (VW1) Adapted with permission from Bauer et al. (2016). ©2016 Elsevier



where 1 million metric tons of  $\text{CO}_2$  were injected between November 2011 and November 2014. Figure 1b shows a map of the Illinois Basin Decatur Project. Figure 2b shows a detailed map with the location of Verification Well 1 (VW1). The specimens in this investigation came from Verification Well 1. Figure 2a shows a profile of Mt. Simon sandstone formation. The Mt. Simon sandstone formation comprises three sections: the Upper Mt. Simon sandstone formation, ranging from 5526 to 5890 ft, the Middle Mt. Simon sandstone formation ranging from 5890 to 6401 ft, and the Lower Middle Mt. Simon sandstone formation ranging from 6401 to 7000 ft (Freiburg et al. 2014).

## 2.2 Experimental Program

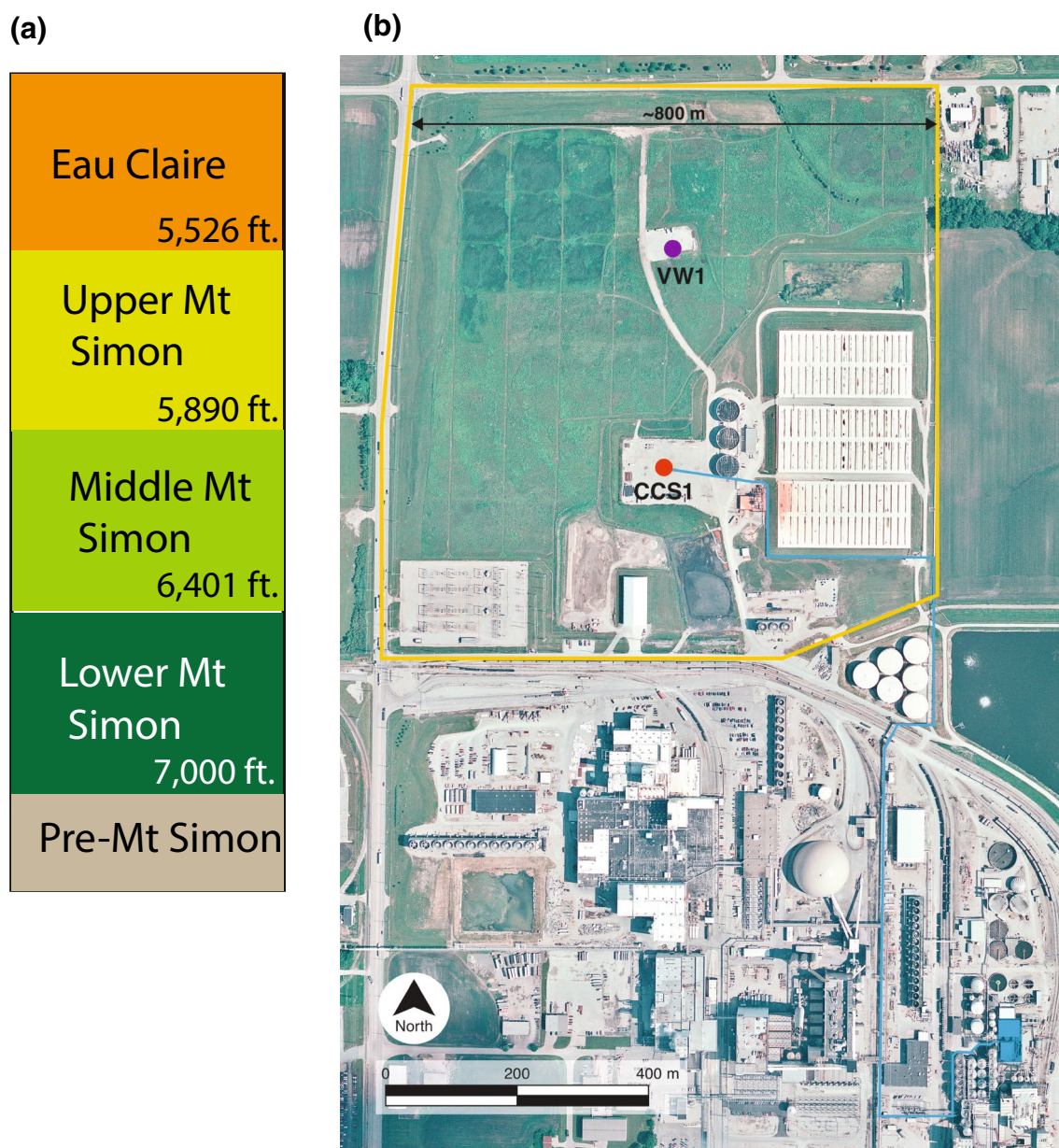
The cores tested in this study came from the Lower Middle Mt. Simon sandstone formation. The cores were extracted at depth 2110.7 m (6925 ft) and at depth 2111.3 m (6927 ft) below ground. Figure 1a shows a digital photographic image of the unaltered Mt. Simon sandstone core extracted at a depth of 6925 ft. After extraction, the cores were sealed and preserved at 4 °C at the Illinois State Geological Survey core repository facility until further examination.

Figure 3 details our experimental program. Two virgin cores were extracted from the Mt. Simon sandstone formation at depths 6925 and 6927 ft. The 6925 ft core was then sub-sampled into five subsamples: four of those subsamples were reserved for incubation experiments. Incubation took place in four acidic systems:

- Brine A, brine B, and brine C for 2 weeks at room temperature, 22 °C, and atmospheric pressure, 0.1 MPa. Brine recipe A, brine recipe B, and brine recipe C correspond to three different synthetic brine solutions. The solutions differ in their ionic strength and in their concentration of NaCl, KCl, and MgCl. In particular, brine recipe A exhibits a low ionic strength, 2.44, brine recipe B exhibits a medium ionic strength, 3.76, and brine recipe C exhibits the highest ionic strength, 4.87. The brine solutions were found to be slightly acidic with a pH of 5, as measured by a pH probe. The exact composition of each solution is given in Table 1.
- $\text{CO}_2$ -saturated brine at 2500 psi and 50 °C for 7 days. The experimental set-up for  $\text{CO}_2$  incubation is presented in detail in Fuchs (2017). Moreover, similar experimental set-ups have been described in the scientific literature (Marbler et al. 2013; Rathnaweera et al. 2015; Tudek et al. 2017; Wang and Clarens 2012).

In terms of testing:

- X-ray diffraction, scanning electron microscopy, and mercury intrusion porosimetry tests were carried out on the unaltered 6925 ft. Mt. Simon sandstone subsample, 6925-U.
- Flow perporometry experiments were carried out on specimens coming from the samples 6925-U, 6927-U, and 6925-AS1, which correspond, respectively, to Mt. Simon sandstone from depth 6925 ft. in a virgin state,



**Fig. 2** **a** Profile of Mt. Simon sandstone formation. **b** Location of Verification Well 1, where the Mt. Simon sandstone cores were extracted from Reprinted with permission from Locke et al. (2013). ©2013 Elsevier

Mt. Simon sandstone from depth 6927 ft. in a virgin state, and Mt. Simon sandstone from depth 6925 ft. after a 7-day incubation in  $\text{CO}_2$  at 2500 psi and  $50^\circ\text{C}$ .

- Grid indentation was performed on all specimens. Table 2 summarizes the grid indentation testing protocol, the number of grids, and the number of tests in each grid. For each grid, the spacing between the indentation locations was  $20\ \mu\text{m}$ . Six samples were studied, corresponding to two depths— 6925 and 6927 ft. from Verification

Well 1—and four alteration regimens (brine recipes A–C), and  $\text{CO}_2$ -saturated brine for 7 days. A total of 24 specimens were tested and 6900 individual indentation tests were carried out. Two types of indentation grids were chosen:  $10 \times 10$  yielding 100 indents and covering a  $180 \times 180\ \mu\text{m}$  area, and  $20 \times 20$  yielding 400 indents and covering a  $380 \times 380\ \mu\text{m}$  area.

**Fig. 3** Experimental program. *HP* helium pycnometry tests, *MIP* mercury intrusion porosimetry tests, *SEM/EDS* scanning electron microscopy/electron-dispersive spectroscopy tests, *XRD* X-ray diffraction tests

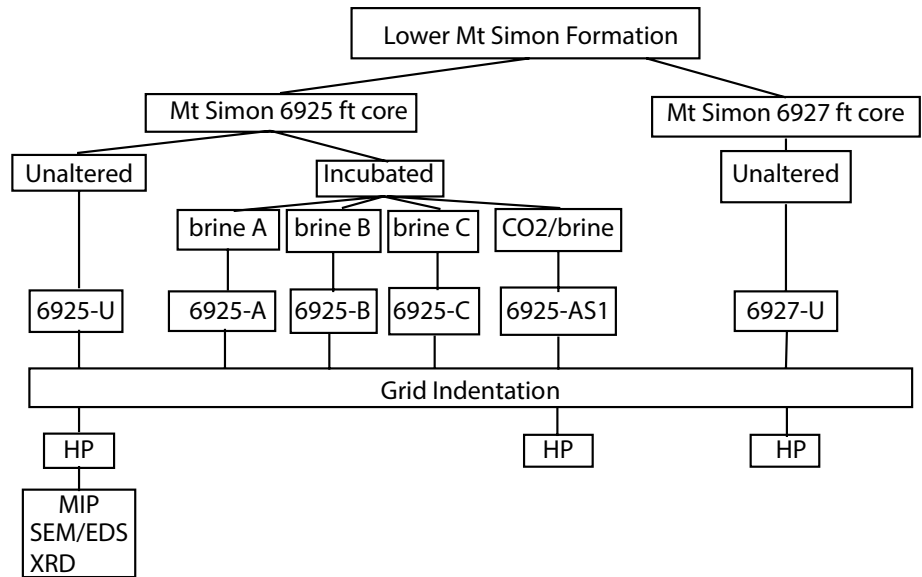


**Table 1** Chemical composition of brine solutions

Chemical concentration (g/l)	Brine A	Brine B	Brine C	Brine D
NaCl	37.47	111.6	74.95	111.67
CaCl <sub>2</sub> · 2H <sub>2</sub> O	24.37	78.35	48.74	78.35
MgCl <sub>2</sub> · 6H <sub>2</sub> O	8.36	16.52	16.73	16.52
KCl	75.00	4.31	150.00	0.00
SrCl <sub>2</sub> · 6H <sub>2</sub> O	0.06	2.37	0.12	2.37
LiCl	1.21	9.36	2.43	9.36
KBr	0.00	0.00	0.00	6.48
Na <sub>2</sub> SO <sub>4</sub>	0.00	0.00	0.00	0.48
pH	5	5	5	
Ionic strength	2.44	3.76	4.87	

*Brine A* moderate concentration—lowest ionic strength, *Brine B* high sodium chloride content—medium ionic strength, *Brine C* high potassium chloride—highest ionic strength. Brine D was used for incubation with CO<sub>2</sub> at high pressure and high temperature

### 2.3 Microstructural Observations

We used scanning electron microscopy (SEM), environmental scanning electron microscopy (ESEM), and X-ray energy-dispersive spectroscopy (EDS) to understand the fabric and composition of the Mt. Simon sandstone. Scanning electron microscopy and back-scattered electron microscopy studies were conducted at the Frederick Seitz Materials Science Laboratory and Microscopy Suite of the Beckman Institute Imaging Group at the University of Illinois at Urbana-Champaign using a JEOL 6060 LV and a FEI Quanta FEG 450, respectively. Scanning electron microscopy was performed at low vacuum (1 Torr) without coating the specimens. The accelerating voltage ranged from 15 to 20 kV with the working distance ranging from 6 to 10 mm, and the magnification levels ranging from 100 to 10000X.

A lapping and polishing procedure was developed to yield a surface finish with tight tolerances in the nanometer range. A major challenge was the heterogeneous nature of the Mt.

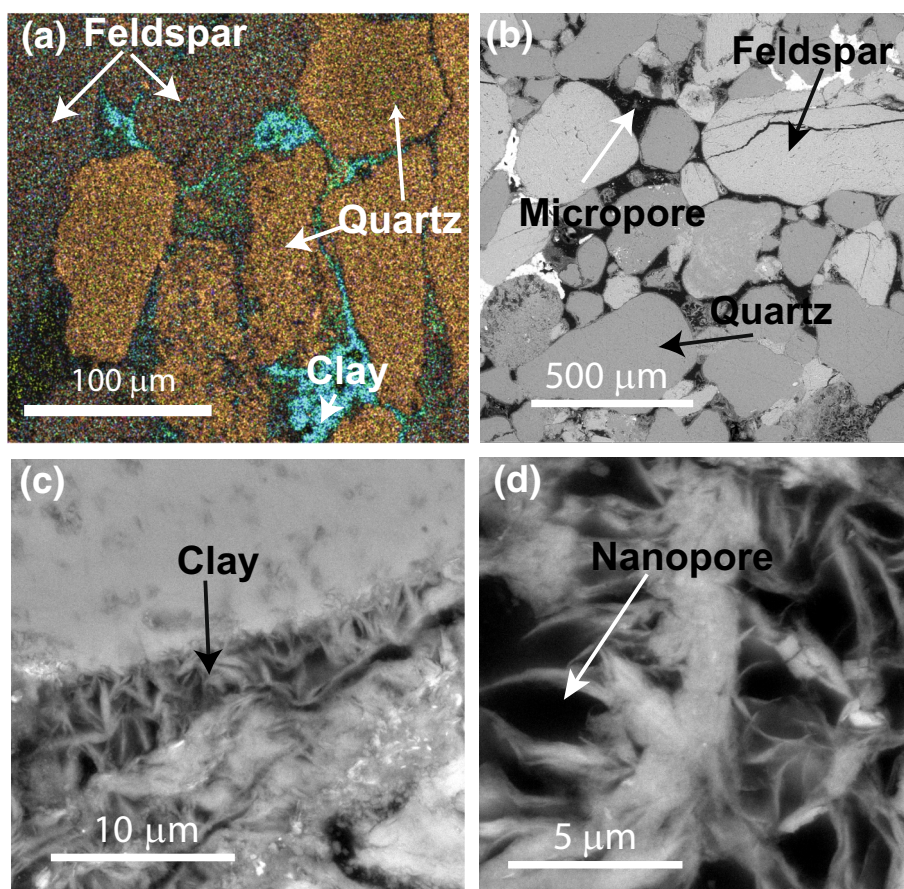
**Table 2** Incubation and testing protocols utilized in this study

Specimen	Fluid	Incubation time	Temperature	Pressure	# of indentation grids	# tests per grid
6927-U	N. A.	N. A.	N. A.	N. A.	4	100, 400
6925-U	N. A.	N. A.	N. A.	N. A.	6	100, 400
6925-A	Brine A	14 days	22 °C	15 psi	3	400
6925-B	Brine B	14 days	22 °C	15 psi	2	400
6925-C	Brine C	14 days	22 °C	15 psi	4	400
6925-AS1	sc CO <sub>2</sub> + Brine D	7 days	50 °C	2500 psi	5	400

Nanoindentation tests performed in this study. A total of 24 specimens were tested with 6900 individual indentation tests carried out on six different samples

*U* unaltered sample. *sc* CO<sub>2</sub> supercritical liquid CO<sub>2</sub>

**Fig. 4** **a** Electron-dispersive X-ray fluorescence image of an unaltered Mt. Simon sandstone 6925 ft. specimen showing feldspar and quartz grains. **b** Back-scattered scanning electron image of an unaltered Mt. Simon sandstone 6925-ft specimen showing K-feldspar (light gray) and quartz (dark grain) grains along with micropores (in black). **c, d** Back-scattered scanning electron images of an unaltered Mt. Simon sandstone 6925-ft specimen showing clay nanosheets surrounding grains with nanopores present within clay



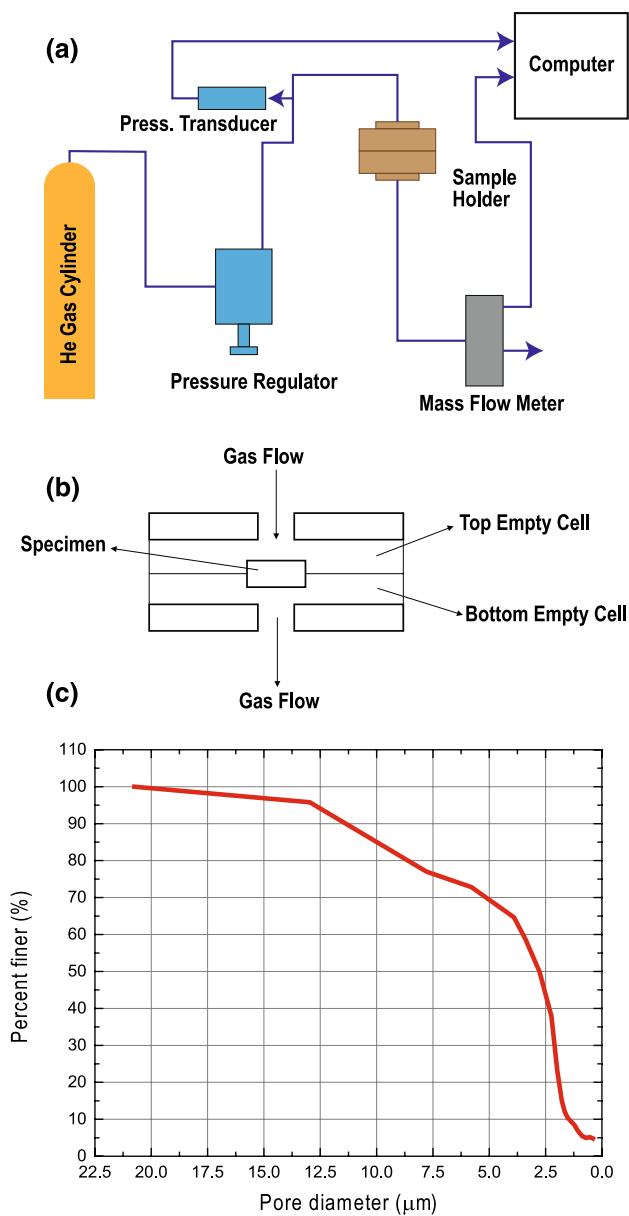
Simon sandstone. The first step was sawing using a linear precision diamond saw. Next, a lapping and polishing system with a specimen jig was used at various speeds and pressures. Abrasive silicon carbide clothes were used to remove the subsurface damage induced by grinding. Polishing was carried out using hard perforated chemo-textiles and oil-based colloidal diamond suspensions with different gradations: 9, 3, 1 and 0.3  $\mu\text{m}$ . Optical microscopy was employed to monitor scratches, pitting, and relief. In between each step, the surfaces were cleansed using an ultrasonic bath in a chemically-inert solvent. After polishing, the quality of our procedures was assessed using atomic force microscopy (AFM). The average root mean squared surface roughness over a  $25 \times 25 \mu\text{m}$  area for a polished Mt. Simon sandstone specimen was less than 30 nm, which is small compared to the lowest penetration depths recorded, 80 nm. A small surface roughness with regard to the penetration depth is important to accurately measure the local elasto-plastic properties.

Figure 4 displays an electron-dispersive X-ray fluorescence image and back-scattered scanning electron microscopy (BSE) images of unaltered Mt. Simon sandstone specimens in the bedding plane at magnification levels ranging from 100 to 10000X. Figure 4a, b shows a granular and heterogeneous microstructure with K-feldspar and quartz

grains. For instance, in Fig. 4b K-feldspar grains are shown in light gray, whereas quartz grains are shown in dark gray. The grain size ranges from 50 to 500  $\mu\text{m}$ . Figure 4b shows the presence of 10–100  $\mu\text{m}$  micropores in the inter-granular space. Figure 4c, d shows clay nanosheets around the grain with nanopore sizes of 500–2000 nm in diameter. Thus, we observe a two-scale porosity. Therefore, Mt. Simon sandstone exhibits a porous, granular, and multiphase microstructure, which needs to be included in the theoretical multiscale model.

## 2.4 Porosity Measurements

The pore size distribution and the pore volume fraction were measured using flow perporometry, helium pycnometry, and mercury intrusion porosimetry. A detailed description of helium pycnometry can be found in Nia et al. (2016). Flow perporometry is a powerful technique commonly used to assess the pore size distribution (PSD) of rock specimens. The underlying principle is capillary flow theory: for a given pore that is wetted by a liquid, the pressure required to force gas through the pore is inversely proportional to the size of the pore, as described by the Laplace equation:



**Fig. 5** **a** Schematic of the flow perporometry experiment. **b** Schematic of specimen holder for flow perporometry experiment. **c** Example of pore size distribution for a specimen 6925-U as measured via flow perporometry

$$r = \frac{2\sigma \cos \theta}{\Delta p}, \tag{1}$$

where  $r$  is the pore radius,  $\sigma$  is the liquid surface tension, and  $\Delta p$  is the prescribed pressure drop.

Figure 5a shows a schematic of our flow perporometry experiment and Figure 5b shows a schematic of the specimen holder. In our experiments, a rock specimen was placed in the specimen holder in between two empty cells. To relate the flow rate to the pressure drop for the dry specimen,

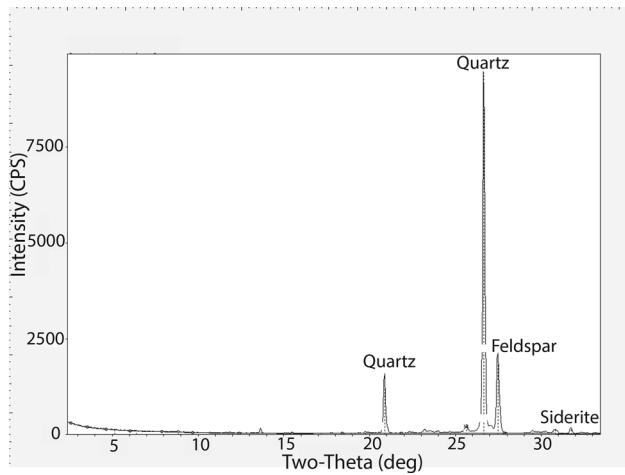
helium gas was pressurized in the top cell at a given pressure high enough to induce flow through the specimen. The flow rate and upstream pressure were recorded simultaneously as the pressure was increased stepwise. Next, the relation between flow rate and pressure drop for the wet specimen was assessed as follows. After wetting the specimen with *n*-butanol, the rock specimen was reinstalled in the apparatus. The top cell was again pressurized with helium, but this time the liquid in the pores acted as a barrier, and no flow occurred until the applied pressure reached the capillary pressure of the largest pores (see Eq. (1)). As the pressure was increased stepwise, more liquid was expelled from progressively smaller and smaller pores, thus allowing more gas to permeate. The experimental data were analyzed using ASTM D6767 (2016) to generate the pore size distribution.

Figure 5c displays an example of pore size distribution for a specimen from sample 6925-U as measured using flow perporometry. The pore diameter  $2r$  spans two orders of magnitude from 200 to 20 μm. Nanopores, with a diameter less than 1780 nm, represent less than 15% of the total porosity. Helium pycnometry revealed a porosity of  $\phi = 25.8 \pm 0.50\%$  for the sample 6925-U and a porosity of  $\phi = 21.30 \pm 1.90\%$  for the sample 6927-U (Mt. Simon sandstone extracted from 6927 ft. and in unaltered state). Meanwhile, mercury intrusion porosimetry revealed a porosity of  $\phi = 21.43\%$  for the sample 6925-U (Mt. Simon sandstone extracted from 6925 ft. and in an unaltered state).

### 2.5 X-ray Diffraction Analysis

X-ray powder diffraction was carried out at the Fredrick Seitz Materials Research Laboratory in collaboration with the Illinois State Geological Survey to determine the mineralogical composition of Mt. Simon sandstone. Each specimen was cleaned and dried in a vacuum oven. Afterward, each specimen was mechanically ground down to an even particle size of around 44 microns. The resulting powder was then spread on a glass slide and characterized using a Siemens/Bruker D5000 X-ray Powder Diffraction instrument. JADE™ software was utilized to identify the constituents and percentages in Mt. Simon sandstone using XRD pattern.

XRD analyses were carried out on unaltered Mt. Simon sandstone specimens extracted from a depth of 6925 ft. (6925-U). Figure 6 displays the corresponding X-ray diffractogram. X-ray diffraction analysis revealed four major constituents of Mt. Simon sandstone, listed in Table 3: quartz (57%wt), alkali feldspar (35 %wt), siderite (5 %wt), and clay (1 %wt). In addition, there were some traces of other minerals such as dolomite and pyrite (2 %wt). The dominant clay minerals were illite (55% in weight), illite/smectite (33% in weight), and chlorite (10% in weight). These findings are congruent with previous XRD analyses carried out on Mt.



**Fig. 6** X-ray diffractogram of an unaltered Mt. Simon specimen extracted at a depth of 6925 ft. below ground

Simon sandstone (Freiburg et al. 2014; Yoksoulian et al. 2013).

The volume fraction  $c_i$  for each mineral  $i$ — $i = \{\text{clay, quartz, feldspar, siderite}\}$ —was computed as follows:

$$c_i = \frac{(\%wt_i)}{\rho_i} \frac{(1 - \phi)}{\frac{(\%wt_{\text{clay}})}{\rho_{\text{clay}}} + \frac{(\%wt_{\text{quartz}})}{\rho_{\text{quartz}}} + \frac{(\%wt_{\text{feldspar}})}{\rho_{\text{feldspar}}} + \frac{(\%wt_{\text{siderite}})}{\rho_{\text{siderite}}}}, \tag{2}$$

where  $\rho_i$  is the density of each mineral as reported in the scientific literature,  $(\%wt_i)$  is the weight fraction as assessed using X-ray diffraction analyses, and  $\phi$  is the porosity at the microscopic scale.

Given the porosity and the density of the different minerals, we can estimate the volume fraction of minerals from the XRD measurements as shown in Table 3. The XRD analyses will serve as a benchmark to check the ability of statistical nanoindentation to yield accurate representations of the mineralogical composition.

### 2.6 Grid Indentation Testing

Grid indentation was carried out on both altered and unaltered samples. In general, grids of indentation were carried out on three to four specimens per sample as detailed in Table 2. The sample origin is given in Fig. 3. A total of 24 specimens were tested and 6900 individual indentation tests were performed.

Statistical nanoindentation or grid indentation testing is commonly employed to infer a map of the chemo-mechanical constituents of rocks (Zhu et al. 2009), shale (Abedi et al. 2016; Akono and Kabir 2016), and cementitious materials (Sorelli et al. 2008; Ulm et al. 2007). The basic principle is to identify the microscopic phases by representing the experimental probability density functions of the local elasto-plastic characteristics using a Gaussian mixture model. Herein, all tests were carried out using an Anton Paar nano-hardness tester (Anton Paar, Ashland, VA, USA). Engineering controls were enforced to avoid common pitfalls of nanoindentation such as excessive thermal drift, high instrument compliance, and inaccurate indenter geometry characterization. For instance, an optical breadboard was used to isolate the instrument from floor vibrations. An enclosure chamber was integrated with a stiff frame, materials with low thermal expansion were used, and cutting-edge

**Table 3** Physical properties of unaltered Mt. Simon sandstone as measured via X-ray diffraction, helium pycnometry, and mercury intrusion porosimetry

		6927-U				
Porosity (%)	HP	Neutron porosity log				
		21.30±1.90	18.7*			
		6925-U				
Porosity (%)	HP	MIP	Neutron porosity log			
		25.80±0.50	21.43	18.7–22**		
X-ray diffraction	Quartz	K-feldspar	Siderite	Clay	(Pyrite, Dolomite)	
	(% wt)	57	35	5	1	2
density (gcc)		2.65	2.56	3.96	2.75	2.71
vol. frac. (%)		45.01	28.61	2.64	0.76	1.54

HP helium pycnometry, MIP mercury intrusion porosimetry, vol. frac. volume fraction

\*Source: (Frailey et al. 2011)

\*\*Source: (Frailey et al. 2016; Bauer et al. 2016)



data acquisition systems were utilized. High-accuracy force and depth sensors were employed with a resolution of 0.01  $\mu\text{N}$  and 0.01 nm, respectively. The force and penetration depth were monitored every 70 ms. The indenter probe was a diamond Berkovich tip with a 2 nm radius and the contact area of the probe was calibrated prior to testing using a reference material. Due to a close integration between the indentation testing unit and advanced imaging optics, it was possible to accurately select the location of each indentation grid.

Figure 7 displays a typical horizontal force–penetration depth curve recorded during an indentation test on a Mt. Simon sandstone specimen. As shown in the insert, during an individual test, the vertical force  $P$  was linearly increased up to a maximum value of  $P_{\text{max}} = 5$  mN, held constant for 5 s and then linearly decreased. The local indentation modulus  $M$  (respectively, indentation hardness  $H$ ) was computed

from the measured unloading contact stiffness  $S$  (respectively, penetration depth  $d_{\text{max}}$  at maximum load) according to the Oliver and Pharr model (Oliver and Pharr 1992, 2004):

$$M = \frac{\sqrt{\pi}}{2} \frac{S}{A(d_{\text{max}})}; \quad H = \frac{P_{\text{max}}}{A(d_{\text{max}})}. \quad (3)$$

Herein,  $P_{\text{max}} = 5$  mN is the prescribed maximum force, and  $A$  is the projected contact area when the maximum load is reached. Similarly,  $d_{\text{max}}$  is the value of the penetration depth when  $P = P_{\text{max}}$ .

## 3 Theory

### 3.1 Multiscale Model of Mt. Simon Sandstone

A conceptual multiscale model was formulated for the Mt. Simon sandstone to connect the local behavior at the nano- and microscopic lengthscales to intrinsic properties at the macroscopic scale. An important challenge is to account for the multiscale nature of Mt. Simon sandstone, the two-scale porosity, the aspect ratio of grains, as well as the heterogeneous nature of the mineral phase. These observations stem from the BSE and XRD analyses. First, X-ray powder diffraction analyses revealed three major mineral phases—quartz (57%wt), feldspar (35%wt), and siderite (5%wt), see Fig. 6. These different mineral phases are also present in the EDS scan and can be observed according to their gray level in the BSE images, see Fig. 4. Thus, at the microscopic scale, the solid skeleton is heterogeneous. Second, high-resolution SEM shows the presence of nanopores, see Fig. 4. Third, the grains shown in Fig. 4 are not spherical.

Figure 8 illustrates our conceptual model. At the molecular lengthscale, the elementary phase is a K-feldspar mineral. The elastic properties of the solid skeleton are characterized by a bulk modulus  $k_s$  and a shear modulus  $g_s$ . At the nanometer lengthscale or nanopore lengthscale, the representative elementary volume consists of solid feldspar with uniformly dispersed nanopores. At lengthscale I, both the nanopores and feldspar nanograins are assumed to be spherical. At the microscale or pore lengthscale, the material is modeled as a granular multi-phase solid. The different phases consists of grains made of quartz, siderite, nanoporous feldspar, and microscopic air voids. At lengthscale II, the grains are modeled as oblate spheroids and the particle aspect ratio  $\alpha$  is accounted for. At the macroscopic scale, the core lengthscale, the material is modeled as a homogeneous isotropic solid. Our goal is to bridge lengthscale 0 and lengthscale III using statistical nanoindentation coupled with micromechanics modeling.

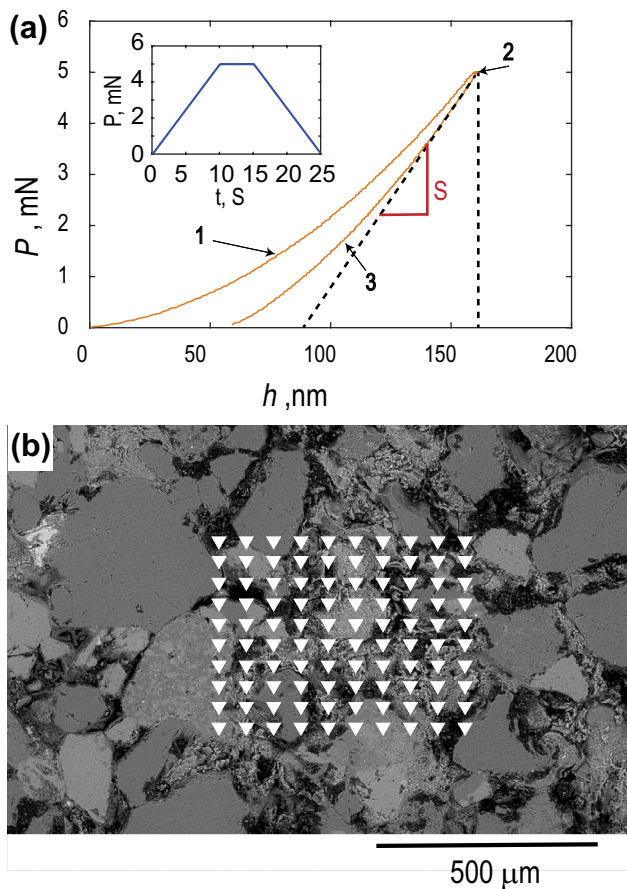


**Fig. 7** **a** Representative load–depth curve for an indentation test performed on Mt. Simon sandstone. The prescribed load history is shown in the insert. **b** Grid of indentations on a Mt. Simon sandstone specimen visualized using scanning electron microscopy.  $P$  is the vertical force,  $d$  is the penetration depth.  $t$  is the time,  $S$  is the unloading contact stiffness

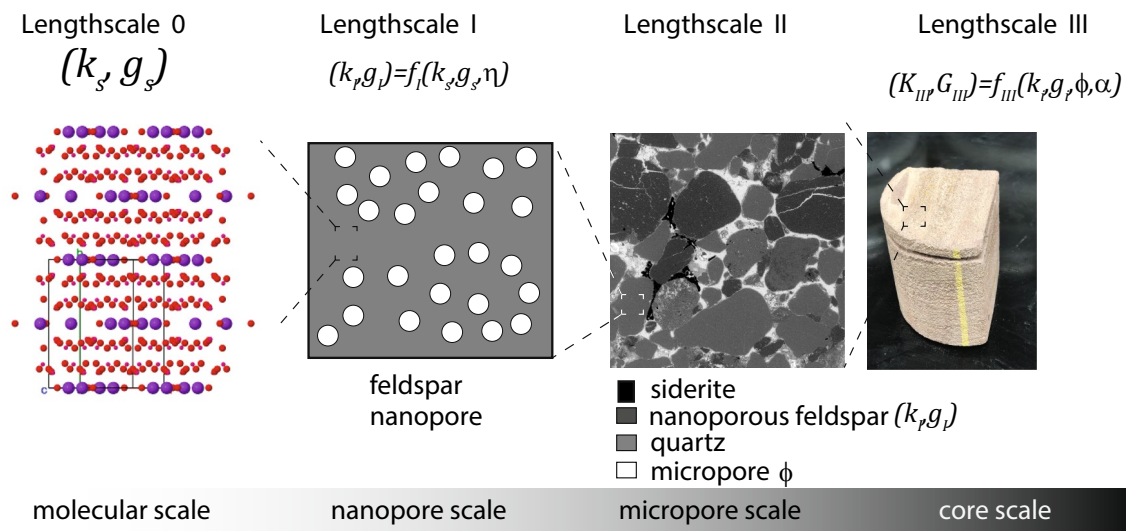


**Fig. 8** Multiscale model of Mt. Simon sandstone. Lengthscale 1: solid feldspar with nanoporosity. Lengthscale 2: heterogeneous grains of quartz, siderite, micropores, and nanoporous feldspar domain. Lengthscale 3: homogeneous material response at macroscopic lengthscale

## 3.2 Elasticity and Strength Upscaling Models

### 3.2.1 Lengthscale 0 to Lengthscale I

Linear upscaling is utilized to connect the molecular scale, lengthscale 0, to the nanopore scale, lengthscale I. At the nanoscale, we represent a nanoporous feldspar phase as a two-phase solid: a solid skeleton and nanoscale air voids, as shown in Fig. 8. We express the bulk modulus and shear modulus at lengthscale I, respectively,  $k_I$  and  $g_I$  as a function of the local packing density  $\eta$  and as a function of the elastic constants of the solid skeleton: bulk modulus  $k_s$  and shear modulus  $g_s$ . The stiffness tensor of the solid skeleton is then given by  $\mathbb{C} = 3k_s\mathbb{J} + 2g_s\mathbb{K}$ .  $\mathbb{J} = \frac{1}{3}\mathbf{1} \otimes \mathbf{1}$  is the fourth-order spherical projector tensor, where  $\mathbf{1}$  is the second-order unit tensor and  $\otimes$  denotes the dyadic product. Meanwhile,  $\mathbb{K} = \mathbb{I} - \mathbb{J}$  where  $\mathbb{I}$  is the symmetric fourth-order unit tensor. We use a micromechanics-based Mori–Tanaka scheme (Nemat and Nasser 1999; Mori and Tanaka 1973). When the reference phase is the matrix, the homogenized stiffness tensor at lengthscale I,  $\mathbb{C}_I$ , is given by Zaoui (2002):

$$\mathbb{C}_I = \eta\mathbb{C}_s : \mathbb{A}_s, \quad (4)$$

$\mathbb{A}_s = \left[ \mathbb{I} + (\mathbb{I} - \mathbb{P}_s : \mathbb{C}_s)^{-1} \right]^{-1}$  is the strain concentration tensor for the solid phase. The tensor  $\mathbb{S}$  is closely related to the Eshelby tensor:  $\mathbb{P} = \mathbb{S} : \mathbb{C}_s^{-1}$ . The Eshelby tensor for a spherical inclusion (here a nanopore) embedded in a linear elastic homogeneous medium (here feldspar) reads (Eshelby 1957):

$$\mathbb{S} = \frac{3k_s}{3k_s + 4g_s}\mathbb{J} + \frac{6(k_s + 2g_s)}{5(3k_s + 4g_s)}\mathbb{K}. \quad (5)$$

By replacing both the Eshelby tensor and the strain concentration tensor by their relative expressions in Eq. (4), we can rewrite the homogenized stiffness tensor at lengthscale I as  $\mathbb{C}_I = 3k_I\mathbb{K} + 2\mu_I\mathbb{J}$ , where  $k_I$  and  $g_I$  are, respectively, the lengthscale I bulk and shear modulus. We can show that  $k_I$  and  $g_I$  are given by:

$$k_I = \frac{4}{3} \frac{\eta k_s g_s}{(1 - \eta)k_s + 4\mu_s} \quad (6)$$

$$g_I = \frac{\eta(9k_s + 8g_s)g_s}{(6(1 - \eta) + 9)k_s + (12(1 - \eta) + 8)g_s}. \quad (7)$$

The plane strain modulus is then calculated using  $M_I = 4g_I \frac{3k_I + g_I}{3k_I + 4g_I}$ .

### 3.2.2 Lengthscale II to Lengthscale III

The next step is to link the micropore scale, lengthscale II, to the macroscopic scale, lengthscale III. Our objective is to estimate the macroscopic bulk modulus  $K_{III}$  and the macroscopic shear modulus  $G_{III}$  knowing the characteristics of microphases at the pore lengthscale. At lengthscale II, the morphology is granular with the different inclusions corresponding to siderite, quartz, nanoporous feldspar and micropores. It is important to account for the granular morphology by considering the grain aspect ratio  $\alpha$ . To account for the aspect ratio of the grains, we utilize the self-consistent solutions for ellipsoidal inclusions formulated by Berryman (1980). Consider a particulate composite with  $n$  phases so that each phase  $i$  is characterized by a bulk modulus  $k_i$ , a shear modulus  $g_i$ , and a volume fraction  $c_i$ , the effective

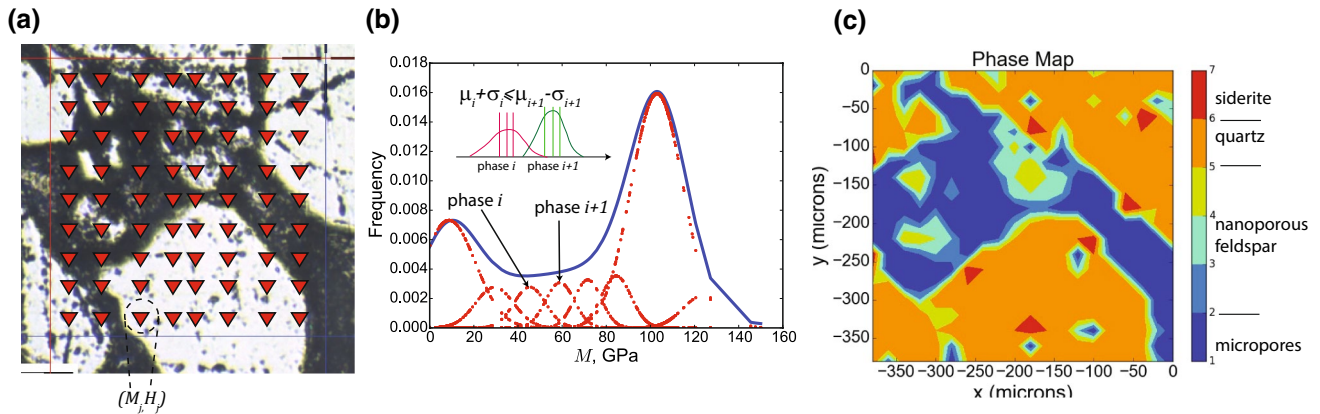


**Fig. 9** **a** Schematic of an indentation grid on a Mt. Simon sandstone specimen. **b** Distribution of indentation modulus  $M$ . The solid line is the experimental probability distribution function. The dotted lines are the theoretical individual Gaussian functions identified via statis-

tical deconvolution. **c** Phase map displaying the spatial arrangement of the individual mechanical phases. The chemical phases can be identified based on the mechanical signature of silicate minerals, See Table 4

elastic constants ( $K_{III}, G_{III}$ ) of the composites are solutions of the implicit equation (Berryman 1980):

$$\sum_i c_i(k_i - K_{III})P^{*i} = 0; \quad \sum_i c_i(g_i - G_{III})Q^{*i} = 0. \tag{8}$$

In the case of oblate particles of aspect ratio  $\alpha$ , the parameters ( $P^{*i}, Q^{*i}$ ) are defined as

$$P^{*i} = \frac{K_{III} + \frac{4}{3}g_i}{k_i + \frac{4}{3}g_i + \pi\alpha\beta_{III}} \tag{9}$$

$$Q^{*i} = \frac{1}{5} \left( 1 + \frac{8G_{III}}{4g_i + \pi\alpha(G_{III} + 2\beta_{III})} + 2 \frac{k_i + \frac{2}{3}g_i + \frac{2}{3}G_{III}}{k_i + \frac{4}{3}g_i + \pi\alpha\beta_{III}} \right), \tag{10}$$

where  $\beta_{III} = G_{III} \frac{3K_{III} + G_{III}}{3K_{III} + 4G_{III}}$ . Equations (8)–(9) are solved using an iterative scheme as described in Berryman (1980).

Thus, we have formulated a multiscale linear homogenization scheme to upscale the elastic properties of Mt. Simon sandstone while accounting for (i) the dual porosity, (ii) the heterogeneous nature of the mineral phase, and (iii) the aspect ratio of particles at the microscopic scale. Equipped with a vast array of characterization methods along with rigorous theoretical models, we can study the influence of rock–fluid reactions on the mechanical response.

### 3.3 Statistical Gaussian Mixture Model

Statistical nanoindentation was carried out at lengthscale II to yield a map of mechanical phases as shown in Fig. 9c. A Gaussian mixture model is employed to identify mineralogical phases based on their mechanical signature (indentation modulus  $M$  and indentation hardness  $H$ , and packing density

$\eta$ ), cf. Fig. 9a. Finite mixture modeling is a powerful method widely employed in a vast range of disciplines such as computer vision (Zivkovic 2004), speech recognition (Yu and Deng 2016), and medical imaging (Bousse et al. 2012).

Given a vector  $\mathbf{X}$  of independent local mechanical characteristics, the idea is to represent the experimental probability distribution function of  $X$  as a weighted sum of individual micro-constituents. For instance, we can define a two-dimensional space  $\mathbf{X} = (M, H)$  where,  $M$  and  $H$  are, respectively, the indentation modulus and hardness that are evaluated using Eq. (3). We can also define a three-dimensional space  $\mathbf{X} = (M, H, \eta)$ , where the packing density  $\eta$  is included as a means to obtain valuable information regarding the morphology. Let us assume the existence of  $n$ -independent micro-constituents within the representative elementary volume at the microscopic scale. The micro-constituents may differ in both their chemistry and their morphology. For each individual micro-constituent,  $i$ , the vector of mechanical and physical properties  $\mathbf{X}_i$  is a two-dimensional or three-dimensional continuous random variable. We assume that the probability density function of  $\mathbf{X}_i$  obeys a multivariate Gaussian distribution characterized by a mean vector  $\boldsymbol{\mu}_i$  and a diagonal covariance matrix  $\boldsymbol{\Sigma}_i$ . Therefore, we can write the probability density function of  $\mathbf{X}_i$  as:

$$p_{\mathbf{X}_i}(\mathbf{X}) = \mathcal{N}(\mathbf{X}, \boldsymbol{\mu}_i, \boldsymbol{\Sigma}_i) = \frac{1}{\sqrt{(2\pi)^k |\det \boldsymbol{\Sigma}|}} \times \exp \left[ -\frac{1}{2} (\mathbf{X} - \boldsymbol{\mu}_i)^T \boldsymbol{\Sigma}^{-1} (\mathbf{X} - \boldsymbol{\mu}_i) \right], \tag{11}$$

where  $k = 2, 3$  is the dimensionality of variable  $\mathbf{X}$ .  $\det \boldsymbol{\Sigma}$  is the determinant of the covariance matrix  $\boldsymbol{\Sigma}$ .  $\mathcal{N}$  denotes the normal distribution function. The next step is to represent the probability distribution function of the population of measured local mechanical properties— $\mathbf{X} = (M, H)$  or

**Table 4** Mechanical signature of silicate minerals present in Mt. Simon sandstone

Mineral	M(GPa)	References
Quartz	79.1	McSkimin et al. (1965)
Quartz	98.1	McSkimin et al. (1965)
Quartz	80.8	Heyliger et al. (2003)
Quartz	103.8	Heyliger et al. (2003)
Feldspar	44.4	Carmichael (1989)
Feldspar	69.6–81.7	Waesermann et al. (2016)
Siderite	146.0	Christensen (1972)
Siderite	169.0	Christensen (1972)

*M* elastic plane strain modulus

$\mathbf{X} = (M, H, \eta)$ —as a combination of sub-populations corresponding to the microphases. We minimize the difference between the experimental probability distribution function  $f_{\mathbf{X}}(\mathbf{X})$  and the weighted sum of individual Gaussian distributions:

$$\min_{c_i, \mu_i, \Sigma_i} \left( f_{\mathbf{X}}(\mathbf{X}) - \sum_{i=1}^n c_i \mathcal{N}(\mathbf{X}, \mu_i, \Sigma_i) \right)^2, \quad (12)$$

with the constraints:

$$c_i \geq 0, 1 \leq i \leq n; \quad \sum_{i=1}^n c_i = 1. \quad (13)$$

$c_i$  represents the volume fraction of phase  $i$ . Eq. (13) states that the volume fraction of each individual phase must be positive and the sum of all volume fractions for all identified mechanical phases must be equal to unity. For simplicity, we require the covariance matrices  $\Sigma_j$  to be diagonal.

In addition, we enforce the phase separability condition, illustrated in Fig. 9b. In other words, we require sufficient contrast between neighboring phases and sufficient difference between neighboring peaks. This condition is encapsulated in the inequality below:

$$\mu_{x_i} + \sigma_{x_i} \leq \mu_{x_{i+1}} - \sigma_{x_{i+1}} \quad (14)$$

with  $x \in \{M, H, \eta\}$ . As illustrated in Fig. 9b, we require the peaks to be sufficiently distinct. Furthermore, to prevent spurious phases, we enforce threshold values on the volume fractions as well as the bandwidth: respectively,  $c_i \geq 5\%$ , and  $\sigma_{x_i} \geq 0.05\mu_{x_i}$ , with  $x \in \{M, H, \eta\}$ . The threshold value is necessary to prevent spurious phases; however, due to that constraint, we are not yet able to account for clay phases.

Thus, in a two-dimensional space,  $X = (M, H)$ , the input of the statistical deconvolution procedure is the distribution  $(M_i, H_j)_{1 \leq i, j \leq N}$  of indentation moduli and hardness values measured locally at individual indentation points. The outcome is the micro-constituents, or mechanical phases  $i$  as

characterized by their volume fraction  $c_i$ , the average and standard deviation of their indentation modulus,  $\mu_{Mi} \pm \sigma_{Mi}$  and indentation hardness  $\mu_{Hi} \pm \sigma_{Hi}$ . Furthermore, in a three-dimensional space, the input of the statistical deconvolution procedure is the distribution  $(M_j, H_j, \eta_j)_{1 \leq i \leq N}$  of indentation modulus, indentation hardness, and packing density values measured locally at individual indentation points.  $\eta_j$  is the local packing density which is computed using Eqs. (6)–(7). The outcome is the micro-constituents, or mechanical phases  $i$  as characterized by the values of the volume fraction  $c_i$ , the average and standard deviation of the indentation modulus,  $\mu_{Mj} \pm \sigma_{Mj}$ , and indentation hardness,  $\mu_{Hj} \pm \sigma_{Hj}$ , and the average and standard deviation of the packing density,  $\mu_{\eta_j} \pm \sigma_{\eta_j}$ . Furthermore, as shown in Fig. 9c, given the spatial location of individual indents, we can draw a map of the mechanical phases.

The mineralogical phases are identified based on their mechanical signature. Table 4 lists the mechanical properties of feldspar, quartz, and siderite as reported in the scientific literature based on experiments such as ultrasonic wave velocimetry (Christensen 1972) and resonance ultrasound spectroscopy (Heyliger et al. 2003), or based on theoretical modeling (Waesermann et al. 2016). Siderite exhibits the highest values with  $M$  ranging from 146.0 to 169.0 GPa. For quartz,  $M$  varies between 79.1 and 103.8 GPa. Quartz minerals are generally modeled as transversely isotropic with the highest value of  $M$  being recorded in the longitudinal direction and the lowest value being in the transverse direction. Feldspar exhibits the broadest range of values with literature reports ranging from 44.4 to 81.7 GPa. Hence, statistical deconvolution of grid indentation data enables us to visualize the spatial arrangement of mineralogical phases.

### 3.4 Modeling Strategy

Figure 10 illustrates our strategy to connect geochemical reactions to the morphological changes that they generate and the resulting alterations in mechanical properties. The first step consists of carrying out a statistical deconvolution for each indentation grid. For each indentation grid, each indentation test will yield one value of the indentation hardness and one value of the indentation modulus computed from the 1000 data points present in the load–depth curve using Eq. (3). The probability density functions of the indentation modulus and indentation hardness are computed using kernel density estimation. The Gaussian mixture parameters are estimated by nonlinear constrained optimization of Eq. (4) using a Python nonlinear solver on an Intel(R) Xeon(R) CPU E5-2609 v4 processor. The output is a map of the mechanical phases present within the specimen, both non-porous (quartz and siderite), and porous (micropores and nanoporous feldspar). Next, we filter and separate the data points  $(M_j, H_j)$  laying within porous phases.

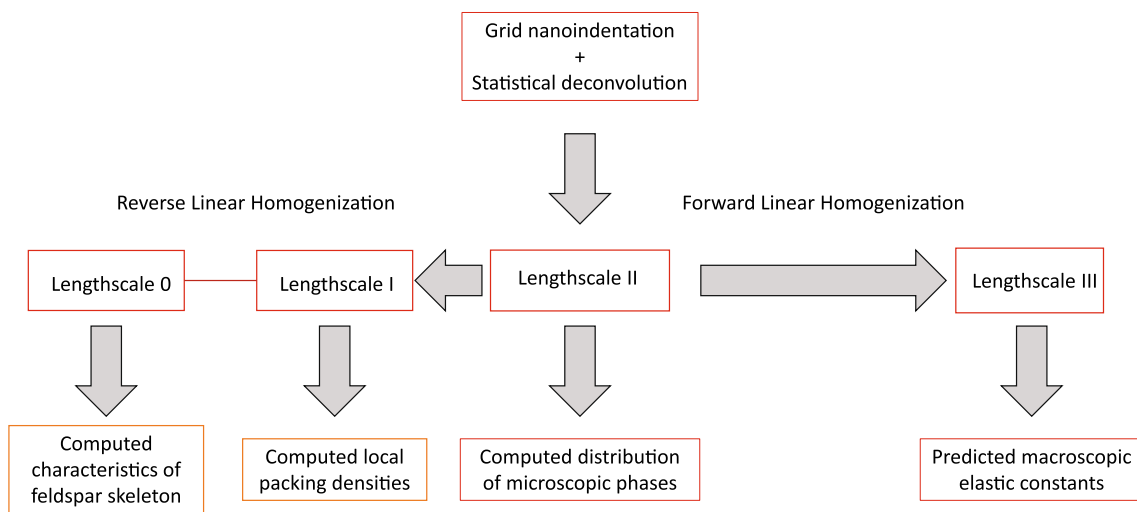


**Fig. 10** Modeling strategy to connect morphological and compositional changes induced by geochemical reactions to macroscopic geomechanical alterations

A subsequent inverse linear homogenization based on Eqs. (6)–(7) yields the local packing densities  $\eta_i$  at lengthscale I. In addition, statistical deconvolution is carried out solely for points laying within porous phases with  $X = (M, H, \eta)$  so as to increase our resolution and better differentiate between microporosity and nanoporous feldspar phases of different packing density values.

Thus, at the end of the two-step statistical deconvolution analysis, we obtain a full picture of Mt. Simon sandstone at lengthscale II for the distribution of minerals and lengthscale I for the local packing densities. At this stage, a forward linear homogenization is carried out using Eq. (8) to predict the effect of compositional and morphological changes on the macroscopic elastic constants. Using the theoretical steps outlined, we can quantify the microstructural changes due to fluid–rock interactions and predict their effect on the effective behavior at the macroscopic lengthscale.

Figure 11 illustrates the statistical deconvolution steps on a representative Mt. Simon sandstone specimen. We set threshold values to match mechanical phases with chemical compounds based on the mechanical signature of silicate minerals present in the Mt. Simon sandstone. For values of the average indentation modulus  $\mu_{Mi}$  above 105 GPa, the mechanical phase  $i$  is considered to be siderite like. For values of  $\mu_{Mi}$  between 78 GPa and 105 GPa, the mechanical phase is considered to be quartz like. For values of  $\mu_{Mi}$  between 20 and 78 GPa, the mechanical phase is considered to be feldspar like.

In Fig. 11, two phases are identified with average indentation moduli in the range 20–78 GPa: these phases correspond to two nanoporous feldspar sub-phases with different packing density values. Similarly, two phases are identified with average indentation moduli in the range 78–105 GPa;

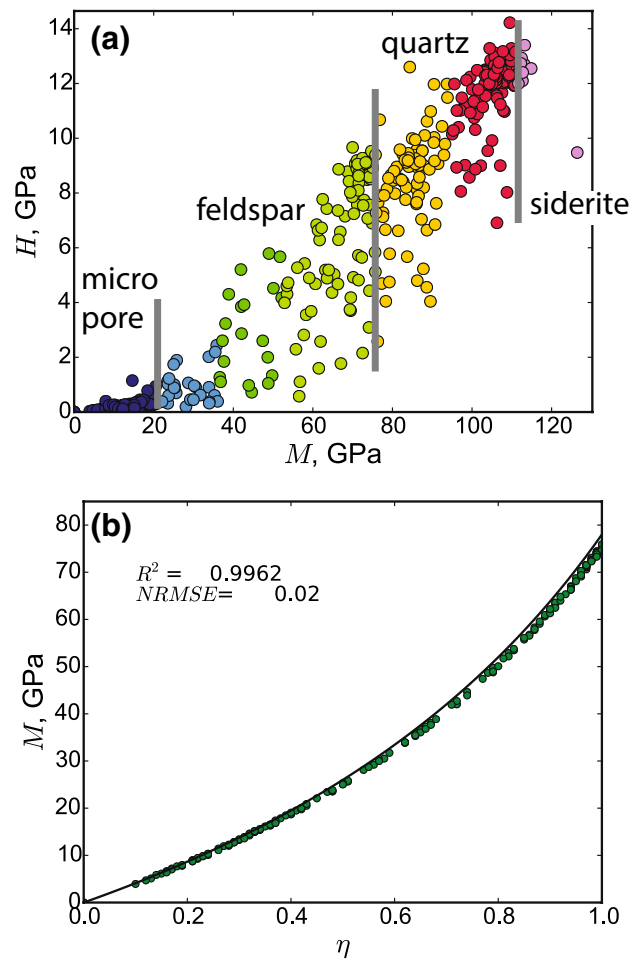


**Fig. 11** **a** Example of statistical deconvolution on Mt. Simon sandstone. **b** Typical indentation modulus–packing density curve

**Table 5** Comparison of porosity values predicted using the statistical nanoindentation method versus experimental measurements

Specimen	SNI	HP	Neutron porosity log	MIP
6927-U	23.38 ± 1.48	21.30 ± 1.90	18.7–22 <sup>a</sup>	
6925-U	23.61 ± 6.86	25.80 ± 0.50	18.7–22 <sup>a</sup>	21.43

HP helium pycnometry, SNI statistical nanoindentation, MIP mercury intrusion porosimetry

<sup>a</sup>Source: (Frailey et al. 2011; Bauer et al. 2016)

these are more likely quartz crystals with different orientations. At lengthscale 0, the elastic constants of the solid feldspar skeleton were calculated as  $k_s = 41.56 \pm 1.76$  GPa and  $g_s = 31.17 \pm 1.32$  GPa. Figure 11b displays the indentation modulus–packing density curve. The solid line represents the theoretical indentation modulus for a nanoporous material as derived in Eq. (7). A close agreement is observed between theory and experiment as evidenced by the high coefficient of determination  $R^2 = 0.99262$  and the low normalized root mean squared error NRMSE = 0.02.<sup>1</sup>

## 4 Results and Discussion

### 4.1 Verification of Multiscale Framework Using Independent Chemical and Microstructural Characterization Methods

We validate our statistical deconvolution approach on unaltered Mt. Simon sandstone by comparing the porosity and mineral content estimates with the results of independent experimental approaches such as X-ray diffraction analysis, mercury intrusion porosimetry, helium pycnometry, and neutron porosity well logs. For instance, Table 5 displays the results of porosity measurements for two unaltered samples: 6925-U extracted from a depth of 6925 ft and 6927-U extracted from a depth of 6927 ft. The porosity values presented in Table 5 using grid indentation are the average values computed for four to six different indentation grids, each involving 100 or 400 indentation tests per grid as described in Table 2. The average porosity values calculated for 6927-U and 6925-U using statistical nanoindentation are

<sup>1</sup> The normalized root mean squared error is defined as

$$\text{NRMSE} = \frac{\sqrt{\frac{\sum_{i=1}^N (\hat{y}_i - y_i)^2}{N}}}{y_{\max} - y_{\min}}$$

where  $(y_i)_{1 \leq i \leq N}$  are the experimental data points and  $(\hat{y}_i)_{1 \leq i \leq N}$  is the theoretical prediction.

**Table 6** Comparison of mineralogy computed via the statistical nanoindentation method with XRD measurements

Mineralogy (% wt)	Quartz	Feldspar	Siderite
SNI	41.67 ± 8.18	33.02 ± 13.46	3.50 ± 4.79
XRD	45.01	28.61	2.64

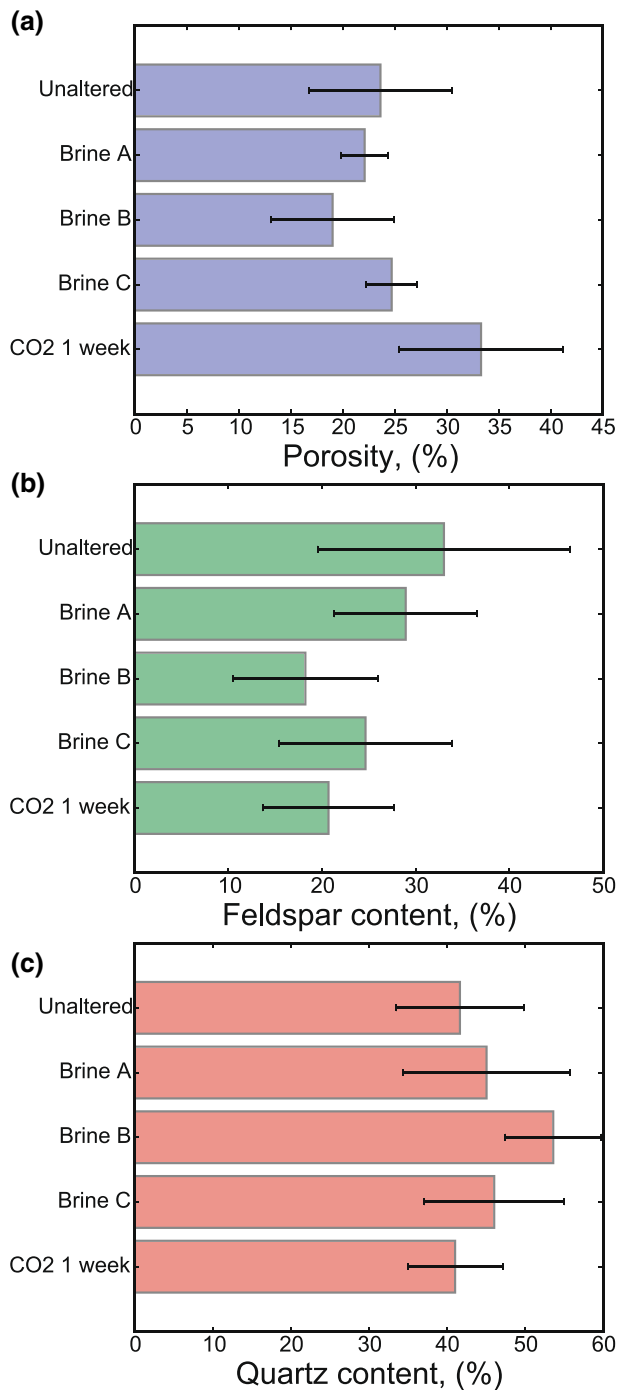
23.38 and 23.61%, respectively, which are in good agreement with independent porosity measurements.

Table 6 summarizes the volume fractions of minerals estimated for the 6925-U sample using statistical nanoindentation. The average quartz volume content calculated for 6925-U is 41.67%, which is in good agreement with the quartz volume content from XRD, 43.69%. In addition, the average feldspar volume content estimated via SNI is 33.02%, which agrees well with the XRD measurements of 28.61%. Finally, the average siderite volume content calculated is 3.50 % using statistical nanoindentation compared to 2.56% from XRD measurements. The difference between XRD measurements and advanced cluster analysis is partially due to the presence of clay particles, pyrite, and dolomite which are represented in the XRD analysis. However, our statistical nanoindentation approach considers only quartz, feldspar, and siderite phases. Nevertheless, there is a good agreement between the XRD measurements and our statistical nanoindentation approach. In other words, we have a rigorous method to systematically assess the mineral changes due to geochemical alterations.

### 4.2 Compositional Changes Following Incubation in Acidic Fluid Systems

Figure 12 displays the inferred values of the porosity, feldspar content, and quartz content for Mt. Simon sandstone in both an unaltered and altered states. The different alteration regimens involve incubation in brine, and brine/sc-CO<sub>2</sub>, as described in Sect. 2. Appendix A summarizes the porosity, quartz, and feldspar, and siderite contents calculated by statistical nanoindentation for the 24 different specimens tested and 6900 individual nanoindentation tests carried out, and Appendix B displays the resulting clustering graphs and packing–density curves.

First, moderate changes in porosity and feldspar content are observed for the 14-day incubation cycle in brine at room temperature and under atmospheric pressure. The incubating brine solutions are brine A, brine B, and brine B of, respectively, low, medium, and high ionic strengths. The chemical composition of the brine solutions is given in Table 1. A 5% increase in porosity and a 25% decrease in feldspar content are observed after incubation in brine solutions A, B, and C. However, the quartz fraction remains relatively the same.



**Fig. 12** Changes in **a** porosity, **b** feldspar content, and **c** quartz content for different alteration cycles on Mt. Simon sandstone 6925. The following samples are considered: unaltered (6925-U), incubated in brine recipe A (6925-A), incubated in brine recipe B (6925-B), incubated in brine recipe C (6925-C), and incubated in CO<sub>2</sub>-saturated brine for 1 week (6925-AS1)

Second, significant changes in porosity and feldspar content are observed after incubation in CO<sub>2</sub>-saturated brine. For sample 6925-AS1 that was incubated in brine/

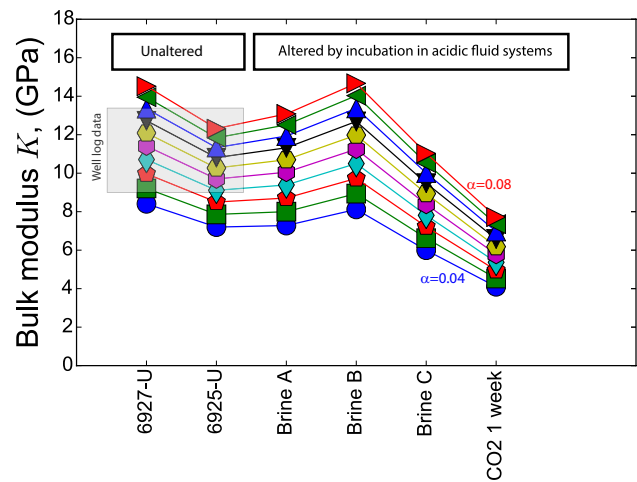


**Fig. 13** Predicted bulk modulus for unaltered and altered Mt. Simon sandstone samples. The value of  $\alpha$  is calibrated based on well log data measurements performed by Bauer et al. (2016). Using the calibrated values of  $\alpha$ , we predict the evolution of the bulk modulus for the altered systems

sc-CO<sub>2</sub> at 50 °C and 2500 psi for 7 days, the feldspar content decreases by 37% and the porosity increases by 41 % from  $23.61 \pm 6.86\%$  in the unaltered state to  $33.28 \pm 7.85\%$  after incubation. A similar result was found using helium pycnometry. However, the magnitude of the increase in porosity was significantly smaller, 1.9%. A plausible reason could be the presence of unconnected porosity. During the dissolution reactions, mineral trapping occurs that obstructs small pore sizes. As a result, the created unconnected pores may not be captured by helium pycnometry.<sup>2</sup>

### 4.3 Resulting Geomechanical Alterations at the Macroscopic Scale

Probing further, we study the influence of the observed compositional and morphological alterations on the mechanical behavior of Mt. Simon sandstone at the macroscopic scale. Given the micro-constituents listed in Table 7, we can estimate the macroscopic elastic constants by application of Eq. (10). A major factor is the aspect ratio of the particle  $\alpha$ .  $\alpha \rightarrow 0$  corresponds to disks and  $\alpha = 1$  corresponds to spheres.

To be more quantitative in our prediction of macroscopic behavior, we need to calibrate the grain aspect ratio  $\alpha$ . To this end, we rely on well log data based on shear wave velocity and compressive wave velocity measurements carried out by Bauer et al. (2016): they reported a bulk modulus of 9.2–13.8 GPa for the lower Mt. Simon sandstone,

<sup>2</sup> There is no clear consensus as to whether helium pycnometry can sense closed-off porosity.

corresponding to the depth range 6920–6940 ft. Based on these values of the bulk modulus, and using the statistical nanoindentation phase calculations, we predict a range of values of  $\alpha = 0.04 - 0.08$  to achieve a quantitative agreement between our macroscopic theoretical predictions and the macroscopic experimental well log data. In turn, the low values of alpha,  $\alpha = 0.04 - 0.08$ , imply that a disk morphology for mineral grains must be adopted to accurately model the constitutive behavior of Mt. Simon sandstone, which points to the importance of the layered structure of the Mt. Simon sandstone formation in dictating the mechanical response.

Figure 13 displays the predicted values of the bulk modulus for Mt. Simon sandstone 6925 ft in the altered states for the range of values  $\alpha = 0.04 - 0.08$ . For a given material, the predicted macroscopic bulk modulus increases as  $\alpha$  increases. Overall, our model predicts a decrease of the bulk modulus as a result of aging in brine or in CO<sub>2</sub>-saturated brine, with CO<sub>2</sub>-saturated brine resulting in the most severe decline in the bulk modulus. In other words, a weakening of the mechanical properties is expected as a result of an increase in porosity and a decrease in feldspar content following the incubation of Mt. Simon sandstone in acidic systems.

#### 4.4 Link Between Incubation-Induced Geochemical Reactions and Geomechanical Alterations

The last step consists of connecting the recorded changes in morphology and mineralogy to the geochemical reactions occurring as a result of the rock interaction with acidic brine or brine saturated with CO<sub>2</sub>. As a guide, we use preliminary studies of geochemical alterations reported for Mt. Simon sandstone. For instance, Yoksoulia et al. (2013) carried out 24-week incubation experiments on Mt. Simon sandstone at 2900 psi and 50 °C and observed an increase in porosity along with an inert behavior of quartz mineral. Our observations are similar to Yoksoulia's and coworkers as we noted an increase in porosity while the quartz content remained constant after incubation in CO<sub>2</sub>-saturated brine. Moreover, based on the kinetic dissolution rates, Yoksoulia et al. predicted a high chemical reactivity for clay and feldspar. As shown in Fig. 12b, we observe a decrease in feldspar content which is accelerated for incubation in CO<sub>2</sub>-saturated brine at temperatures above 50 °C. Thus, in our experiments, our findings suggest a dissolution of feldspar, which results in an increase in porosity and a decrease of the effective bulk modulus. In turn, a higher dissolution rate is observed at

higher temperature, 50 °C vs. 22 °C and for CO<sub>2</sub>-saturated brine solutions.

## 5 Conclusions

We formulated a novel multiscale nanomechanics framework to investigate fluid–rock reactions in Mt. Simon sandstone using statistical nanoindentation integrated with micromechanics modeling. The principle consists of focusing on the mechanical signature of minerals so as to monitor compositional and morphological changes at the nano- and microscopic scales. In turn, using micromechanics upscaling, we can connect these morphological and compositional changes to modifications in the effective mechanical response at the macroscopic scale.

In this study, we investigated geo-chemo-mechanical alterations in Mt. Simon sandstone as a result of incubation in acidic brine as well as CO<sub>2</sub>-saturated brine. 24 different specimens were tested, corresponding to four different alteration cycles and leading to 6900 individual indentation tests. At the microscopic scale, the theoretico-experimental framework was validated by independent techniques such as SEM, EDS, X-ray diffraction, mercury intrusion porosimetry, helium pycnometry, and flow perporometry. At the macroscopic lengthscale, a reasonable agreement was observed with well log data. In our experiments, we observed alkali feldspar dissolution and a porosity increase during incubation regimes in slightly acidic brine and in CO<sub>2</sub>-saturated brine. At the macroscopic lengthscale, a weakening of the rock is predicted. Thus, we have presented a physics-based theoretical and experimental framework to directly tie local changes in composition to macroscopic alterations in the effective mechanical response while accounting for the morphology, heterogeneity and multiscale nature of Mt. Simon sandstone.

**Acknowledgements** This work was supported as part of the Center for Geologic Storage of CO<sub>2</sub>, an Energy Frontier Research Center funded by the U.S. Department of Energy, Office of Science, Basic Energy Sciences under Award # DE-SC0012504. The authors would like to thank the Illinois State Geological Survey for providing the Mt. Simon sandstone specimens tested and analyzed in this investigation. The work was carried out in part in the Frederick Seitz Materials Research Laboratory Central Research Facilities, University of Illinois at Urbana-Champaign.

## Statistical Deconvolution Results

See Table 7.



**Table 7** Summary of porosity, quartz, feldspar, and siderite volume content in % for Mt. Simon sandstone specimens subject to different alteration cycles

Material	$\phi$ (%)	Qtz. (%)	Feldsp. (%)	Sider. (%)	
6927-U	25.92	44.00	28.61	0.00	
	22.38	41.00	40.98	7.00	
	22.83	45.00	36.11	1.00	
	22.39	40.00	41.68	7.00	
Average	23.38	42.50	36.84	3.75	
Std	1.48	2.06	5.22	3.27	
6925-U	30.45	50.00	18.63	1.00	
	31.07	34.00	20.68	14.00	
	21.44	51.00	28.74	1.00	
	28.49	36.00	30.92	2.00	
	16.92	48.00	40.71	0.00	
	13.27	31.00	58.43	3.00	
	Average	23.61	41.67	33.02	3.50
Std	6.86	8.18	13.46	4.79	
6925-A	20.31	56.00	21.44	1.25	
	25.33	30.50	39.40	5.00	
	20.63	48.75	25.98	0.25	
	Average	22.09	45.08	8.94	2.17
Std	2.29	10.73	7.63	2.04	
6925-B	24.94	47.50	26.00	0.75	
	13.07	59.75	10.46	10.50	
	Average	19.01	53.62	18.23	5.62
Std	5.94	6.12	7.77	4.88	
6925-C	25.22	56.00	21.39	1.25	
	27.73	52.75	11.47	1.50	
	24.92	33.25	29.58	9.00	
	20.90	42.25	36.16	8.00	
	Average	24.69	46.06	24.65	4.94
	Std	2.45	8.97	9.23	3.58
6925-AS1	31.61	35.00	15.87	7.25	
	37.93	46.25	12.19	1.00	
	38.90	40.50	19.09	1.25	
	39.36	34.00	23.91	2.00	
	18.62	49.50	32.45	0.25	
	Average	33.28	41.05	20.70	2.35
	Std	7.85	6.08	7.02	2.51

Summary of 6900 indentation tests carried out on 24 specimens

*Qtz.* quartz, *Feldsp.*, *Sider.* siderite,  $\phi$  is the total porosity, 6925-U unaltered, 6925-A= incubation in brine A for 14 days, 6925-B incubation in brine B for 14 days, 6925-C= incubation in brine C for 14 days, 6925-AS1 incubation in brine/sc-CO<sub>2</sub> for 7 days at 50 °C and 2500 psi

## Statistical Deconvolution Graphs

Figures 14, 15 display the indentation modulus–packing density curves for the porous phases on unaltered and altered Mt Simon sandstone specimens. Meanwhile, Figs. 16,

17 display the indentation hardness–indentation modulus graphs for unaltered and altered Mt. Simon sandstone specimens.

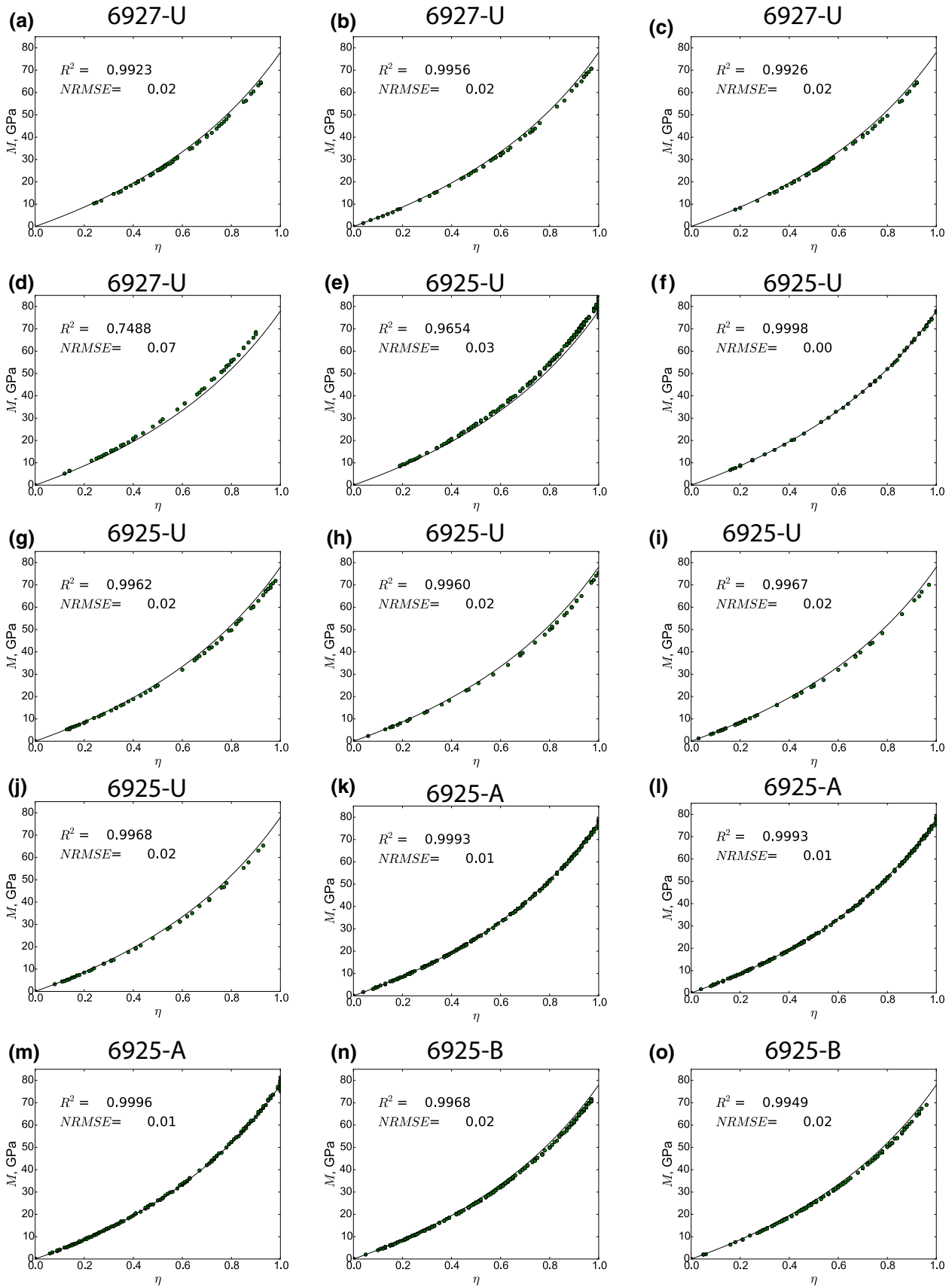


**Fig. 14** Indentation modulus–packing density curves for unaltered and altered Mt. Simon sandstone specimens. **a–d** Unaltered Mt. Simon sandstone 6927-U, **e–j** Unaltered Mt. Simon sandstone 6925-U, **k–m** Mt. Simon sandstone 6925-A incubated in brine A for 14 days at a temperature of 22°C under atmospheric pressure, **n–o** Mt. Simon sandstone 6925-B incubated in brine B for 14 days at a temperature of 22 °C under atmospheric pressure

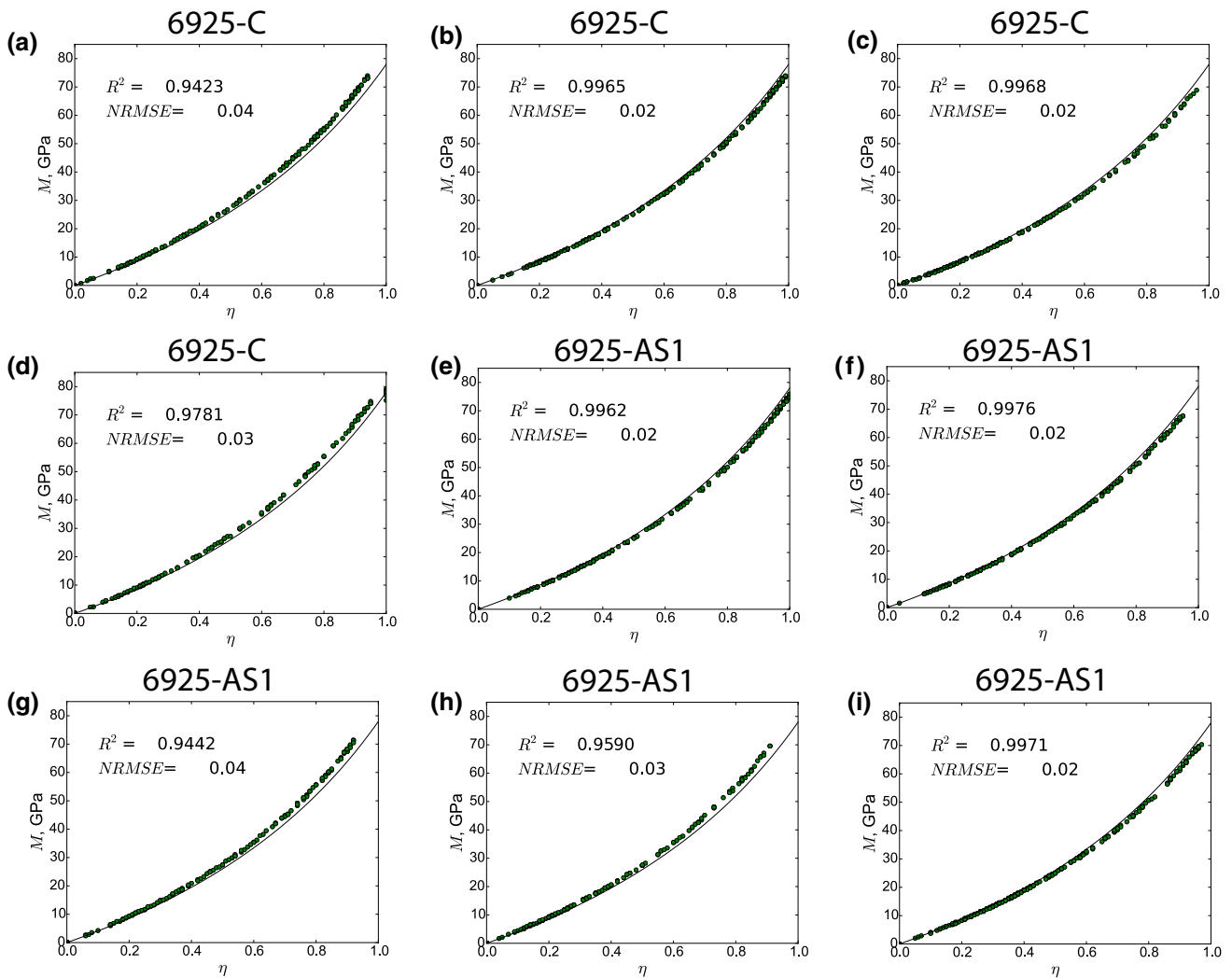


**Fig. 15** Indentation modulus–packing density curves for unaltered and altered Mt. Simon sandstone specimens. **a–d** Mt. Simon sandstone 6925-B incubated in brine C for 14 days at a temperature of

22°C under atmospheric pressure. **e–i** Mt. Simon sandstone 6925-AS1 incubated in brine D saturated with CO<sub>2</sub> for 1 week at a temperature of 50 °C and a pressure of 2500 psi

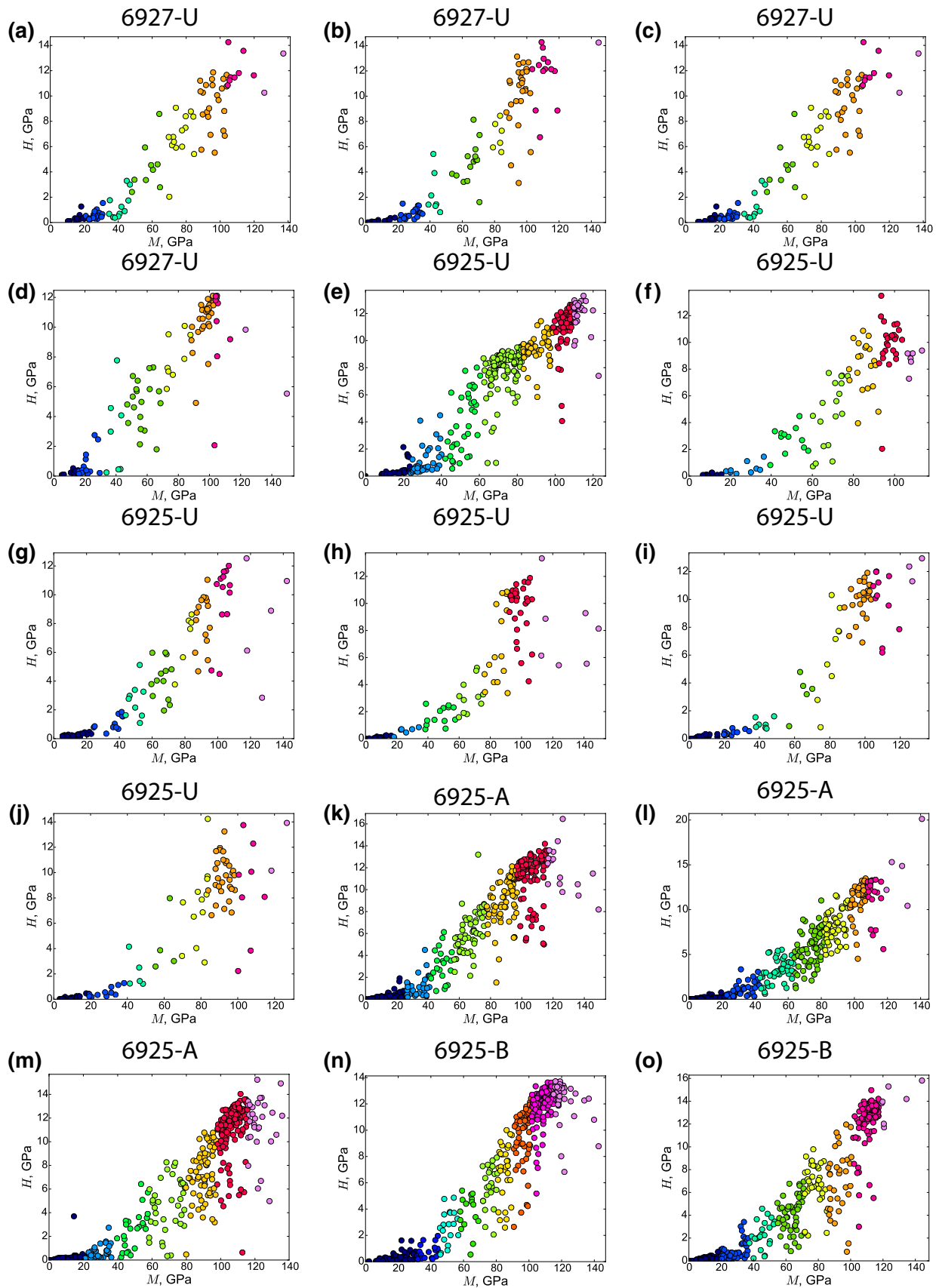


**Fig. 16** Indentation hardness-indentation modulus graphs for unaltered and altered Mt. Simon sandstone specimens. **a–d** Unaltered Mt. Simon sandstone 6927-U, **e–j** Unaltered Mt. Simon sandstone 6925-U, **k–m** Mt. Simon sandstone 6925-A incubated in brine A for 14 days at a temperature of 22 °C under atmospheric pressure, **n–o** Mt. Simon sandstone 6925-B incubated in brine B for 14 days at a temperature of 22 °C under atmospheric pressure

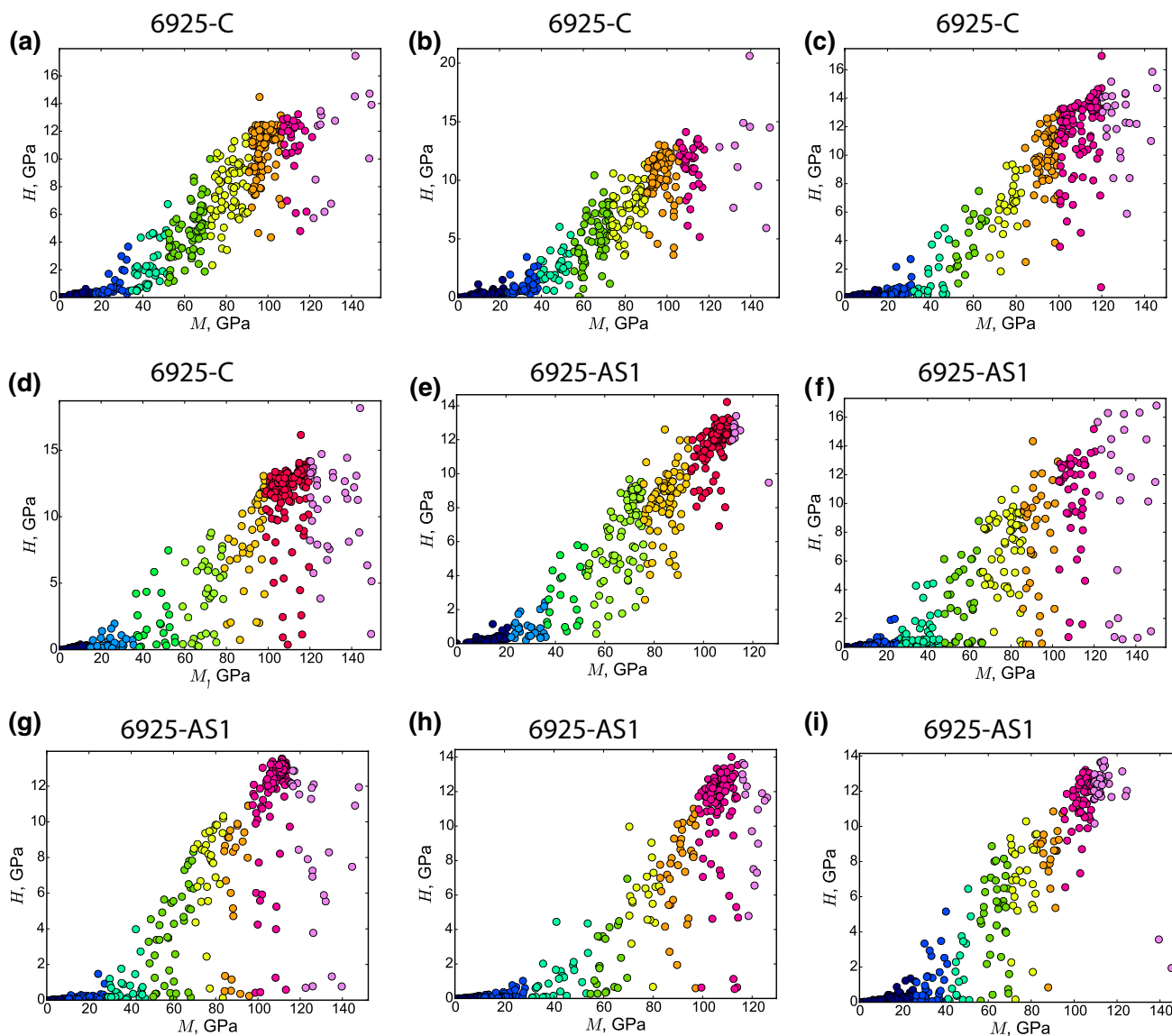


**Fig. 17** Indentation hardness-indentation modulus graphs for unaltered and altered Mt. Simon sandstone specimens. **a–d** Mt. Simon sandstone 6925-B incubated in brine C for 14 days at a temperature

of 22 °C under atmospheric pressure. **e–i** Mt. Simon sandstone 6925-AS1 incubated in brine D saturated with CO<sub>2</sub> for 1 week at a temperature of 50 ° and a pressure of 2500 psi

## References

- Abedi S, Slim M, Hofmann R, Bryndzia T, Ulm FJ (2016) Nanochemomechanical signature of organic-rich shales: a coupled indentation EDX analysis. *Acta Geotechnica* 11(3):559–572
- Akono AT, Kabir P (2016) Nano-scale characterization of organic-rich shale via indentation methods. In: Jin C, Cusatis G (eds) *New frontiers in oil and gas exploration*. Springer, Switzerland, pp 209–233
- Arson C, Vanorio T (2015) Chemomechanical evolution of pore space in carbonate microstructures upon dissolution: linking pore geometry to bulk elasticity. *J Geophys Res Solid Earth* 120(10):6878–6894. <https://doi.org/10.1002/2015JB012087>
- ASTM D6767-16 (2016) Standard test method for pore size characteristics of geotextiles by capillary flow test, ASTM International, West Conshohocken, PA, <https://doi.org/10.1520/D6767-16>
- Bauer RA, Carney M, Finley RJ (2016) Overview of microseismic response to CO<sub>2</sub> injection into the Mt. Simon saline reservoir at the Illinois Basin-Decatur Project. *Int J Greenh Gas Control* 54:378–388
- Bemer E, Lombard JM (2010) From injectivity to integrity studies of CO<sub>2</sub> geological storage-chemical alteration effects on carbonates petrophysical and geomechanical properties. *Oil Gas Sci Technol Revue de l'Institut Français du Pétrole* 65(3):445–459. <https://doi.org/10.2516/ogst/2009028>
- Bemer E, Vincké O, Longuemare P (2004) Geomechanical log deduced from porosity and mineralogical content. *Oil Gas Sci Technol* 59(4):405–426. <https://doi.org/10.2516/ogst:2004028>
- Bethke CM (1996) *Geochemical reaction modeling: concepts and applications*. Oxford University Press, New York
- Berryman JG (1980) Long wavelength propagation in composite elastic media II. Ellipsoidal inclusions. *J Acoust Soc Am* 68(6):1820–1831. <https://doi.org/10.1121/1.385172>
- Bousse A, Pedemonte S, Thomas BA, Erlandsson K, Ourseulin S, Arridge S, Hutton BF (2012) Markov random field and Gaussian mixture for segmented MRI-based partial volume correction in PET. *Phys Med Biol* 57(20):6681. <https://doi.org/10.1088/0031-9155/57/20/6681>
- Carmichael RS (1989) *Physical properties of rocks and minerals*. CRC Press, Boca Raton
- Christensen NI (1972) Elastic properties of polycrystalline magnesium, iron, and manganese carbonate to 10 kilobars. *J Geophys Res* 77(2):369–372. <https://doi.org/10.1029/JB077i002p00369>
- Eshelby JD (1957) The determination of the elastic field of an ellipsoidal inclusion and related problems. *Proc R Soc A* 241:376–396 (JSTOR 100095)
- Frailey SM, Damico J, Leetaru HE (2011) Reservoir characterization of the Mt. Simon Sandstone, Illinois Basin, USA. *Energy Procedia* 4:5487–5494
- Freiburg JT, Morse DG, Leetaru HE, Hoss RP, Yan Q (2014) A depositional and diagenetic characterization of the Mt. Simon Sandstone at the Illinois Basin-Decatur Project Carbon Capture and Storage Site, Decatur, Illinois, USA. Illinois State Geological Survey, Prairie Research Institute, University of Illinois
- Fuchs S (2017) *Geochemical and Geomechanical Alteration of Mt. Simon Sandstone due to Prolonged Contact with CO<sub>2</sub>-saturated Brine during Carbon Sequestration*, Master Thesis, University of Texas Austin
- Gautier JM, Oelkers EH, Schott J (1994) Experimental study of K-feldspar dissolution rates as a function of chemical affinity at 150 C and pH 9. *Geochimica et Cosmochimica Acta* 58(21):4549–4560
- Heyliger P, Ledbetter H, Kim S (2003) Elastic constants of natural quartz. *J Acoust Soc Am* 114(2):644–650. <https://doi.org/10.1121/1.1593063>
- Liteanu E, Spiers CJ (2009) Influence of pore fluid salt content on compaction creep of calcite aggregates in the presence of supercritical CO<sub>2</sub>. *Chem Geol* 265(1–2):134–147
- Locke RL, Larssen D, Salden W, Patterson C, Kirksey J, Iranmanesh A, Wimmer B, Krapac I (2013) Preinjection reservoir fluid characterization at a CCS demonstration site: Illinois Basin-Decatur Project, USA. *Energy Procedia* 37:6424–6433
- Marbler H, Erickson KP, Schmidt M, Lempp C, Pöllmann H (2013) Geomechanical and geochemical effects on sandstone caused by the reaction with supercritical CO<sub>2</sub>: and experimental approach to in situ conditions in deep geological reservoirs. *Environ Earth Sci* 69(6):1981–1998. <https://doi.org/10.1007/s12665-012-2033-0>
- McSkimin HJ, Andreatch JP, Thurston RNL (1965) Elastic moduli of quartz versus hydrostatic pressure at 25 and -195.8 C. *J Appl Phys* 36(5):1624–1632. <https://doi.org/10.1063/1.1703099>
- Nguyen MT, Bemer E, Dormieux L (2011) Micromechanical modeling of carbonate geomechanical properties evolution during acid gas injection. In: 45th US rock mechanics/geomechanics symposium. American Rock Mechanics Association
- Nia SF, Dasani D, Tsotsis TT, Kristian J (2016) An integrated approach for the characterization of shales and other unconventional resource materials. *Ind Eng Chem Res* 55(12):3718–3728. <https://doi.org/10.1021/acs.iecr.5b04761>
- Nover G, Von Der Gönna J, Heikamp S, Köster J (2013) Changes of petrophysical properties of sandstones due to interaction with supercritical carbon dioxide—a laboratory study. *Eur J Mineral* 25(3):317–329. <https://doi.org/10.1127/0935-1221/2013/0025-2295>
- Oliver WC, Pharr GM (2004) Measurement of hardness and elastic modulus by instrumented indentation: advances in understanding and refinements to methodology. *J Mater Res* 19(1):3–20. <https://doi.org/10.1557/jmr.2004.19.1.3>
- Oliver WC, Pharr GM (1992) An improved technique for determining hardness and elastic modulus using load and displacement sensing indentation experiments. *J Mater Res* 7(6):1564–1583. <https://doi.org/10.1557/JMR.1992.1564>
- Rathnaweera TD, Ranjith PG, Perera MSA, Haque A, Lashin A, Al Arifi N, Chandrasekharam D, Yang SQ, Xu T, Wang SH (2015) CO<sub>2</sub>-induced mechanical behaviour of Hawkesbury sandstone in the Gosford basin: an experimental study. *Mater Sci Eng A* 641:123–137. <https://doi.org/10.1016/j.msea.2015.05.029>
- Rimmelé G, Barlet-Gouédard V, Renard F (2010) Evolution of the petrophysical and mineralogical properties of two reservoir rocks under thermodynamic conditions relevant for CO<sub>2</sub> geological storage at 3 km depth. *Oil Gas Sci Technol Revue de l'Institut Français du Pétrole* 65(4):565–580. <https://doi.org/10.2516/ogst/2009071>
- Sorelli L, Constantinides G, Ulm FJ, Toutlemonde F (2008) The nano-mechanical signature of ultra high performance concrete by statistical nanoindentation techniques. *Cem Conc Res* 38(12):1447–1456. <https://doi.org/10.1016/j.cemconres.2008.09.002>
- Sun Z, Espinoza DN, Balhoff MT (2016) Discrete element modeling of indentation tests to investigate mechanisms of CO<sub>2</sub>-related chemomechanical rock alteration. *J Geophys Res Solid Earth* 121(11):7867–7881. <https://doi.org/10.1002/2016JB013554>
- Tudek J, Crandall D, Fuchs S, Werth CJ, Valocchi AJ, Chen Y, Goodman A (2017) In situ contact angle measurements of liquid CO<sub>2</sub>, brine, and Mount Simon sandstone core using micro X-ray CT imaging, sessile drop, and Lattice Boltzmann modeling. *J Pet Sci Eng* 155:3–10
- Ulm F-J, Vandamme M, Bobko C, Alberto Ortega J, Tai K, Ortiz C (2007) Statistical indentation techniques for hydrated nanocomposites: concrete, bone, and shale. *J Am Ceram Soc* 90(9):2677–2692. <https://doi.org/10.1111/j.1551-2916.2007.02012.x>
- Vialle S, Vanorio T (2011) Laboratory measurements of elastic properties of carbonate rocks during injection of reactive

- CO<sub>2</sub>-saturated water. *Geophys Res Lett* 38(1):741–747. <https://doi.org/10.1029/2010GL045606>
- Vanorio T, Ebert Y, Grombacher D (2015) What laboratory-induced dissolution trends tell us about natural diagenetic trends of carbonate rocks. *Geol Soc Lond Spec Publ* 406(1):311–329
- Waeselmann N, Brown JM, Angel RJ, Ross N, Zhao J, Kaminsky W (2016) The elastic tensor of monoclinic alkali feldspar. *Am Mineral* 101(5):1228–1231. <https://doi.org/10.2138/am-2016-5583>
- Wang S, Clarens AF (2012) The effects of CO<sub>2</sub>-brine rheology on leakage processes in geologic carbon sequestration, *Water Resour Res*. <https://doi.org/10.1029/2011WR011220>
- White AF, Brantley SL (2003) The effect of time on the weathering of silicate minerals: why do weathering rates differ in the laboratory and field? *Chem Geol* 202(3–4):479–506
- Yoksoulian LE, Freiburg JT, Butler SK, Berger PM, Roy WR (2013) Mineralogical alterations during laboratory-scale carbon sequestration experiments for the Illinois Basin. *Energy Procedia* 37:5601–5611. <https://doi.org/10.1016/j.egypro.2013.06.482>
- Xie SY, Shao JF, Xu WY (2011) Influences of chemical degradation on mechanical behavior of a limestone. *Int J Rock Mech Min Sci* 48(5):741–747. <https://doi.org/10.1016/j.ijrmms.2011.04.015>
- Yu D, Deng D (2016) Automatic speech recognition. Signals and communication technology. Springer-Verlag, London
- Zaoui A (2002) Continuum micromechanics: survey. *J Eng Mech* 128:808–816
- Zhu W, Fonteyn MTJ, Hughes J, Pearce C (2009) Nanoindentation study of resin impregnated sandstone and early-age cement paste specimens. *Nanotechnol Constr* 3:403–408. <https://doi.org/10.1007/978-3-642-00980-8-55>
- Zinsmeister L, Dautriat J, Dimanov A, Raphanel J, Bornert M (2013) Mechanical evolution of an altered limestone using 2D and 3D digital image correlation (DIC). In: 47th US rock mechanics/ geomechanics symposium
- Zivkovic Z (2004) Improved adaptive Gaussian mixture model for background subtraction. In pattern recognition 2004. ICPR 2004. In: Proceedings of the 17th international conference on (Vol. 2, pp. 28–31). IEEE

**Publisher's Note** Springer Nature remains neutral with regard to jurisdictional claims in published maps and institutional affiliations.